Annual Review of Condensed Matter Physics

The Physics of Pair-Density Waves: Cuprate Superconductors and Beyond

Daniel F. Agterberg,[1] J.C. Séamus Davis,[2,3] Stephen D. Edkins,[4] Eduardo Fradkin,[5] Dale J. Van Harlingen,[6] Steven A. Kivelson,[7] Patrick A. Lee,[8] Leo Radzihovsky,[9] John M. Tranquada,[10] and Yuxuan Wang[11]

[1]Department of Physics, University of Wisconsin-Milwaukee, Milwaukee, Wisconsin 53201, USA

[2]Clarendon Laboratory, University of Oxford, Oxford OX1 3PU, United Kingdom

[3]Department of Physics, University College Cork, Cork T12 K8AF, Ireland

[4]Department of Applied Physics, Stanford University, Stanford, California 94305, USA

[5]Department of Physics and Institute for Condensed Matter Theory, University of Illinois at Urbana-Champaign, Urbana, Illinois 61801, USA; email: efradkin@illinois.edu

[6]Department of Physics, University of Illinois at Urbana-Champaign, Urbana, Illinois 61801, USA

[7]Department of Physics, Stanford University, Stanford, California 94305, USA

[8]Department of Physics, Massachusetts Institute of Technology, Cambridge, Massachusetts 02139, USA

[9]Department of Physics and Center for Theory of Quantum Matter, University of Colorado, Boulder, Colorado 80309, USA

[10]Condensed Matter Physics & Materials Science Department, Brookhaven National Laboratory, Upton, New York 11973, USA

[11]Department of Physics, University of Florida, Gainesville, Florida 32611, USA

Annu. Rev. Condens. Matter Phys. 2020. 11:231–70

The *Annual Review of Condensed Matter Physics* is online at conmatphys.annualreviews.org

https://doi.org/10.1146/annurev-conmatphys-031119-050711

Keywords

intertwined orders, vortex states, finite-momentum condensates, induced orders

Abstract

We review the physics of pair-density wave (PDW) superconductors. We begin with a macroscopic description that emphasizes order induced by PDW states, such as charge-density wave, and discuss related vestigial states that emerge as a consequence of partial melting of the PDW order. We review and critically discuss the mounting experimental evidence for such

PDW order in the cuprate superconductors, the status of the theoretical microscopic description of such order, and the current debate on whether the PDW is a mother order or another competing order in the cuprates. In addition, we give an overview of the weak coupling version of PDW order, Fulde–Ferrell–Larkin–Ovchinnikov states, in the context of cold atom systems, unconventional superconductors, and noncentrosymmetric and Weyl materials.

1. INTRODUCTION

A pair-density wave (PDW) is a superconducting (SC) state in which the order parameter varies periodically as a function of position in such a way that its spatial average vanishes. It is a phase of matter defined in terms of broken symmetries (1–7). In this review, we characterize the macroscopic properties of such a state precisely and discuss the status of the (incomplete) theoretical understanding of the sorts of lattice-scale interactions that give rise to it (the mechanism), how it is distinct from other phases with which it shares certain features, and the way in which the partial melting of the PDW can give rise to daughter phases with a variety of patterns of vestigial order. In addition to its intrinsic interest, there is now evidence that suggests significant (although probably not long-range correlated) PDW order exists in at least some regions of the phase diagram of the cuprate high-temperature superconductors. We critically review this evidence and then speculate on the broader significance of these sightings to the understanding of broader issues in the physics of the cuprates. We also discuss other strongly correlated systems, including other unconventional superconductors, certain cold atom systems, and carefully engineered mesoscopic devices, in which PDW and PDW-related states play an important role.

In a time-reversal- and inversion-invariant Fermi liquid (FL), the SC susceptibilities $\chi_{sc}(\mathbf{q}, T)$ at $\mathbf{q} = \mathbf{0}$ diverge as the temperature lowers toward a critical value. Under some circumstances, there can be a local maximum in $\chi_{sc}(\mathbf{q})$ at nonzero $\mathbf{q}$, but it is always smaller than $\chi_{sc}(\mathbf{0})$. Weak breaking of time-reversal symmetry can change the situation. For example, in the presence of a Zeeman magnetic field, the $T \to 0$ divergence of $\chi_{sc}(\mathbf{0})$ is cut off, with the result that the maximum of χ_{sc} can occur at a wavenumber with $|\mathbf{q}| \sim \epsilon_Z/v_F$, where the Zeeman energy is $\epsilon_z = g\mu_B H$ and v_F is the Fermi velocity. Although there is no longer a strict instability to an SC state at arbitrary weak interactions, under some circumstances such a system can form a finite $\mathbf{q}$ SC phase at low T. This is the long-sought Fulde–Ferrell–Larkin–Ovchinnikov (FFLO) phase (1, 2), which (as we briefly review) has been plausibly shown to exist in certain materials and cold-atom systems.

However, it has been conjectured that, for systems in which the interactions are not weak, a PDW could occur independent of any explicit time-reversal symmetry breaking. In that it does not necessarily break time-reversal symmetry, the PDW is thermodynamically distinct from an FFLO state; that the spatial average of the SC order vanishes distinguishes the PDW from a less exotic phase with simply coexisting charge-density wave (CDW) and SC order. However, though it is straightforward to examine the phenomenological consequences of the existence of a PDW in terms of the standard methods of effective field theory, developing a microscopic theory has proven challenging. It is not favored at weak coupling, and a treatment of the strong coupling problem faces obvious challenges. In this review, we focus on the phenomenological aspects and comment briefly on the microscopic models in Section 5.

Thus, this is less a review of a well-settled subject than a progress report on an interesting, rapidly developing subject. The experimental evidence—especially in the cuprates—is sufficiently dramatic that it cannot be ignored. However, there is not yet the web of consistent evidence from a wide variety of experiments that one would ideally count on to establish the correctness of any particular perspective on the properties of such complex materials. This, combined with the absence

of a reliable microscopic theory, means that a portion of the discussion is necessarily speculative. It is part of what makes the subject so exciting.

2. PHENOMENOLOGICAL THEORY

2.1. Phenomenological Theory: Ginzburg–Landau–Wilson Formulation

The simplest cartoon of a PDW state is one in which the gap function varies sinusoidally as $\Delta(\mathbf{x}) \sim \cos(\mathbf{P} \cdot \mathbf{x})$. As reviewed in Section 3, a state with this spatial dependence and a periodicity of a few lattice spacings was proposed to occur in the cuprate superconductors. This state is similar to the expected FFLO states when a Zeeman magnetic field is applied to a usual, weak-coupling, spin-singlet superconductor (1, 2): The Larkin and Ovchinnikov (LO) state has a similar spatially modulated magnitude, whereas the Fulde–Ferrell (FF) state has a constant magnitude but spatially varying phase, i.e., $\Delta(\mathbf{x}) \sim e^{i\mathbf{P}\cdot\mathbf{x}}$ (8, 9). As noted in the introduction, FFLO phases differ from other PDW states in that, reflecting their origin, they have finite magnetization and long, field-dependent periodicities that are many times the SC coherence length. However, though it has not been emphasized in the previous literature, the same sort of induced subsidiary orders should be expected in an LO state as in a simple PDW, so we treat the two sorts of states simultaneously here.

In general, a PDW state has secondary orders whose existence is dictated by symmetry. These induced orders have played an important role in understanding the relevance of PDW order in the cuprates (4–7, 10–14). Primary among these is CDW order. In addition to exhibiting an induced CDW order, this unidirectional PDW state also has nematic and spatially uniform charge-$4e$ SC orders. These induced order parameters can develop long-range order when the original PDW order does not; the induced order is then often called vestigial order (15). Observation and understanding of this induced order is central to understanding the underlying PDW state. In this section, using a Ginzburg–Landau–Wilson (GLW) approach, we illuminate different types of PDW ground states, the accompanying induced order, and the topological excitations of these states. Because the PDW order breaks translation symmetry in addition to the usual particle number conservation, the topological excitation spectrum is richer than that in usual superconductors. Key to this section is that we assume the existence of an underlying lattice that breaks rotational symmetry. This condition is not true in the context of cold atoms, and this gives rise to different physical properties that are discussed in Section 5.

To be concrete, motivated by the cuprates, we consider a tetragonal system with square lattice sheets stacked along the z-axis. We consider PDW order that exhibits spatial modulations along the in-plane $\hat{x}$ direction. The modulations are assumed to be incommensurate with the lattice. Tetragonal symmetry dictates that the PDW order parameter has four complex degrees of freedom with momenta $\pm\mathbf{P}_x$ and $\pm\mathbf{P}_y$, and the corresponding order parameter is written as $\Delta_i = \{\Delta_{\mathbf{P}_x}, \Delta_{\mathbf{P}_y}, \Delta_{-\mathbf{P}_x}, \Delta_{-\mathbf{P}_y}\}$. These order parameters are coupled to fermions via

$$H_{\mathbf{P}} = \Delta_{\mathbf{P}} \int \mathrm{d}\mathbf{k} F(\mathbf{k}) \mathbf{c}^{\dagger}_{\mathbf{k}+\mathbf{P}/2} \mathbf{c}^{\dagger}_{-\mathbf{k}+\mathbf{P}/2}, \qquad 1.$$

where $F(\mathbf{k})$ is an internal form factor. Note that the form factor is not a representation of a symmetry group, and different form factors, e.g., s wave, d wave, can mix (12). Here, for concreteness, we take an s-wave form factor, so that $\Delta_{\mathbf{P}} = \sum_{\mathbf{k}} g\langle c_{-\mathbf{k}\downarrow} c_{\mathbf{k}+\mathbf{P}\uparrow}\rangle$ (where g is the interaction constant) because different form factors do not alter the essential results discussed in this section, as discussed in Reference 16. The form of the GLW theory then follows from how these order parameters transform under various internal and spatial symmetries. Here, we do not write all such symmetry operations and refer to Reference 16 for a more detailed discussion of these. However, it is worthwhile to highlight some key symmetries that help in understanding the additional

orders that are induced by the PDW order. In particular, under a lattice translation $\mathbf{T}$, the PDW order transforms as $\Delta_{\mathbf{P}} \rightarrow e^{i\mathbf{T}\cdot\mathbf{P}}\Delta_{\mathbf{P}}$. Under time-reversal ($\mathcal{T}$) and parity ($\mathcal{P}$) symmetries, we have

$$\Delta_{\mathbf{P}} \xrightarrow{\mathcal{T}} (\Delta_{-\mathbf{P}})^*, \qquad \Delta_{\mathbf{P}} \xrightarrow{\mathcal{P}} \Delta_{-\mathbf{P}}. \tag{2.}$$

The GLW energy density consistent with time-reversal, parity, space group, and gauge symmetries is (5, 15)

$$\mathcal{H} = \alpha \sum_i |\Delta_{\mathbf{P}_i}|^2 + \beta_1 \Big(\sum_i |\Delta_{\mathbf{P}_i}|^2 \Big)^2 + \beta_2 \sum_{i<j} |\Delta_{\mathbf{P}_i}|^2 |\Delta_{\mathbf{P}_j}|^2 + \beta_3 (|\Delta_{\mathbf{P}_x}|^2 |\Delta_{-\mathbf{P}_x}|^2 \tag{3.}$$
$$+ |\Delta_{\mathbf{P}_y}|^2 |\Delta_{-\mathbf{P}_y}|^2) + \beta_4 [\Delta_{\mathbf{P}_x}\Delta_{-\mathbf{P}_x}(\Delta_{\mathbf{P}_y}\Delta_{-\mathbf{P}_y})^* + (\Delta_{\mathbf{P}_x}\Delta_{-\mathbf{P}_x})^*\Delta_{\mathbf{P}_y}\Delta_{-\mathbf{P}_y}].$$

The parameters β_i depend upon the specific microscopic model. Depending on which values are found for these, one of five possible ground states can be realized. These five phases include the following: (*a*) the FF-type phase with only one momentum component; (*b*) the FF* phase, which is a bidirectional version of the FF-type phase; the LO-type, which includes pairing with opposite momentum components [these include the unidirectional phase and the bidirectional-I and -II phases, which have phase factors of 0 and $\pi/2$ between the two unidirectional components. These five states give rise to different patterns of induced order, providing a means to distinguish them. We now turn to these induced orders.

2.1.1. Induced order parameters. In the context of the cuprates, Ising nematic and CDW order have been the most important of the induced orders. Because the induced CDW order appears often in this review, we discuss it first. CDW order ($\rho_{\mathbf{Q}}$) preserves time-reversal symmetry and breaks translation symmetry and, given two SC order parameters with different pair-density momenta, the CDW order is generally induced as (5–7, 17)

$$\rho_{\mathbf{P}_i-\mathbf{P}_j} \propto (\Delta_{\mathbf{P}_i}\Delta^*_{\mathbf{P}_j} + \Delta_{-\mathbf{P}_j}\Delta^*_{-\mathbf{P}_i}), \tag{4.}$$

where the second term follows from time-reversal invariance. Two important examples of this are (*a*) in the unidirectional PDW state $\rho_{2\mathbf{P}} \propto \Delta_{\mathbf{P}}\Delta^*_{-\mathbf{P}}$ (see **Figure 1*a*** for a real space illustration; note time-reversal symmetry transforms this term into itself) and (*b*) when one of the SC order parameters is translation invariant, then $\rho_{\mathbf{P}} \propto (\Delta_0\Delta^*_{-\mathbf{P}} + \Delta_{\mathbf{P}}\Delta^*_0)$, where Δ_0 is a usual translation invariant SC order. The PDW ground states that are most often discussed with respect to the cuprates are the unidirectional and the bidirectional-II PDW states. This is because these states exhibit CDW order at momentum $2\mathbf{P}_x$ and none at momentum $\mathbf{P}_x + \mathbf{P}_y$, which is consistent with experiments.

Now we turn to the other induced orders. Ising nematic order ($\epsilon_{x^2-y^2}$) that breaks rotational 4-fold symmetry is given by $\epsilon_{x^2-y^2} \propto (|\Delta_{\mathbf{P}_x}|^2 + |\Delta_{-\mathbf{P}_x}|^2 - |\Delta_{\mathbf{P}_y}|^2 - |\Delta_{-\mathbf{P}_y}|^2)$ (6, 17). Magnetization-density wave (MDW) order ($M^z_{\mathbf{Q}}$), which arises from spatially modulated orbital loop currents, is given by $M^z_{\mathbf{P}_i-\mathbf{P}_j} \propto i(\Delta_{\mathbf{P}_i}\Delta^*_{\mathbf{P}_j} - \Delta_{-\mathbf{P}_j}\Delta^*_{-\mathbf{P}_i})$ (5, 7). Translation invariant charge-4*e* SC order (Δ_{4e}) is given by $\Delta_{4e} \propto \Delta_{\mathbf{P}}\Delta_{-\mathbf{P}}$ (10, 17). Uniform charge-4e SC order, a state with $hc/4e$ flux quantization, can occur if the CDW stiffness of the PDW state is sufficiently weak (10) or in continuum systems (where the stripe order melts at any temperature) (18, 19). It may also arise in PDW states with quenched disorder (20). Loop current order (l_i), which is odd under both time-reversal and parity symmetries, but preserves translation symmetry, is given by $l_i \propto (|\Delta_{\mathbf{P}_i}|^2 - |\Delta_{-\mathbf{P}_i}|^2)$ (11). The induced orders appearing in the different PDW ground states are shown in **Table 1**.

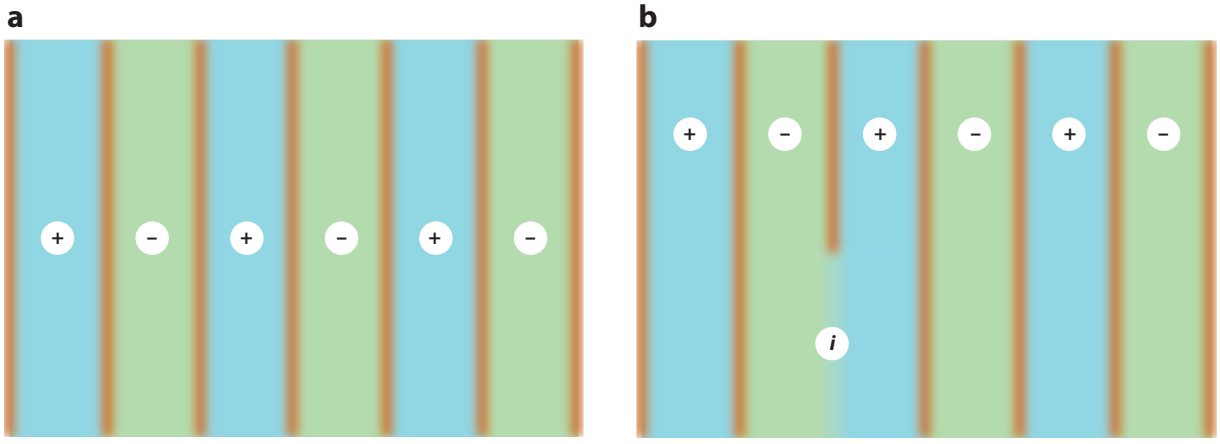

Figure 1

(*a*) Schematic real-space illustration of a unidirectional PDW state (*blue* and *green stripes*) with $\Delta_{\pm\mathbf{P}}$ its induced CDW state (*orange stripes*) $\rho_{\mathbf{Q}=2\mathbf{P}}$. The PDW order parameter changes sign in alternate domains and vanishes at the domain walls, whereas the local density of states is enhanced at the domain walls. The local density of states has a CDW pattern with half the wavelength of the PDW. (*b*) The PDW half vortex, around which the local SC phase winds by π, bound with a CDW dislocation. Abbreviations: CDW, charge-density wave; PDW, pair-density wave; SC, superconducting.

2.1.2. Topological excitations. Just as gauge invariance of the action implies the existence of vortices in usual superconductors, gauge and translation invariance of the Hamiltonian in Equation 3 imply topological excitations in PDW superconductors. Due to breaking of translation symmetry, these PDW topological excitations can exhibit properties that are quite different from usual SC vortices. This is reflected in the appearance of multiple U(1) symmetries that appear in most PDW ground states. Gauge and translation symmetries allow PDW ground states to have up to three U(1) symmetries (one from usual gauge invariance and one each from translation invariance along the $\hat{x}$ and $\hat{y}$ directions). In **Table 1**, these U(1) symmetries are given by the phase factors ϕ_i, which are not determined by minimizing the action. These undetermined phases lead to Goldstone modes, in particular new modes associated with translational symmetry breaking.

Table 1 Pair density wave (PDW) ground states[a]

Phase	$(\Delta_{\mathbf{P}_x}, \Delta_{\mathbf{P}_y}, \Delta_{-\mathbf{P}_x}, \Delta_{-\mathbf{P}_y})$	Induced orders
FF-type	$(e^{i\phi_1}, 0, 0, 0)$	$l_x, \epsilon_{x^2-y^2}$
FF*-type	$(e^{i\phi_1}, e^{i\phi_2}, 0, 0)$	$l_x = l_y$ $\rho_{\mathbf{P}_x-\mathbf{P}_y}, M^z_{\mathbf{P}_x-\mathbf{P}_y}$
Unidirectional	$(e^{i\phi_1}, 0, e^{i\phi_2}, 0)$	$\epsilon_{x^2-y^2}, \Delta_{4e}$ $\rho_{2\mathbf{P}_x}$
Bidirectional-I	$(e^{i\phi_1}, e^{i\phi_2}, e^{i\phi_3}, e^{i[\phi_1+\phi_3-\phi_2]})$	Δ_{4e} $\rho_{2\mathbf{P}_x}, \rho_{2\mathbf{P}_y}, \rho_{\mathbf{P}_x-\mathbf{P}_y}, \rho_{\mathbf{P}_x+\mathbf{P}_y}$
Bidirectional-II	$(e^{i\phi_1}, ie^{i\phi_2}, e^{i\phi_3}, ie^{i[\phi_1+\phi_3-\phi_2]})$	Δ_{4e} $\rho_{2\mathbf{P}_x}, \rho_{2\mathbf{P}_y}\ M^z_{\mathbf{P}_x-\mathbf{P}_y}, M^z_{\mathbf{P}_x+\mathbf{P}_y}$

[a]Distinct PDW ground states and accompanying induced orders. In the third column, other modes can be found by using the relationships $\rho_{\mathbf{Q}} = (\rho_{-\mathbf{Q}})^*$ and $M^z_{\mathbf{Q}} = (M^z_{-\mathbf{Q}})^*$.

These modes are discussed in more detail in Section 5.2. A winding in one or some of these ϕ_i gives rise to the topological excitations.

Physics associated with topological excitations is discussed in detail in References 5, 7, 10, and 17. Here, we focus on the unidirectional (LO) state, which is sufficient to capture the key new physical properties associated with these vortices. Writing $(\Delta_{\mathbf{P}_x}, \Delta_{\mathbf{P}_y}, \Delta_{-\mathbf{P}_x}, \Delta_{-\mathbf{P}_y}) = \Delta(e^{i\phi_1}, 0, e^{i\phi_2}, 0)/\sqrt{2}$, we allow (ϕ_1, ϕ_2) to have a phase winding of (n, m) times 2π, respectively. We call these (n, m) vortices. These vortices are most simply described by the following London theory:

$$\mathcal{H}_L = \frac{1}{2}\sum_{i=x,y,z}\left\{\rho_{s,i}[(\nabla_i\phi_1 - 2eA_i)^2 + (\nabla_i\phi_2 - 2eA_i)^2] + B_i^2\right\}, \qquad 5.$$

where $\rho_{s,i}$ give the superfluid stiffness along these three directions (it is generally anisotropic) and the magnetic field $B = \nabla \times A$. Equation 5 gives rise to a supercurrent with components $J_i \propto \rho_{s,i}[\nabla_i(\phi_1 + \phi_2)/2 - 2eA_i]$. Far from the core of the vortex, the minimum energy configuration has nonzero supercurrent, and a contour integration of this supercurrent then implies that the flux enclosed in an (n, m) vortex is $(n + m)\Phi_0/2$, n and m being the winding number in ϕ_1 and ϕ_2. Consequently, (1, 0) vortices enclose half the usual flux quantum (5). In this description, (1, 1) vortices are the usual single flux quantum Abrikosov vortices. Equation 5 shows that these usual SC vortices typically have the lowest energy because the phase winding can be completely screened by the vector potential, implying that they have a finite energy per unit length. Fractional or zero-flux vortices have an energy per unit length that diverges as the logarithm of the cross-sectional system size.

An examination of the induced CDW order near a $\Phi_0/2$ (1, 0) vortex sheds insight into their physical origin. In particular, the relationship $\rho_{2\mathbf{P}} \propto \Delta_{\mathbf{P}}\Delta^*_{-\mathbf{P}}$ reveals that a dislocation appears in the CDW order due to the phase winding in $\Delta_{\mathbf{P}_x}$. Because this CDW order has half the periodicity of the PDW order, a dislocation in the CDW order corresponds to half a dislocation in the PDW order. Consequently, the half-flux vortex can be seen as a half-dislocation combined with a π phase winding in the PDW order (see **Figure 1*b***). The $\Phi_0/2$ vortices of the other PDW phases have a similar origin. A generic prediction is that a PDW SC vortex containing a half-flux quantum will be pinned to a dislocation in the induced CDW order.

These (n, m) vortices can have some notable physical consequences (5, 7, 10, 17). One example is in fluctuation-driven vortex physics in two dimensions (21–23). In particular, it is possible that the lowest-energy vortex is not a $\Phi_0/2$ (1, 0) vortex but either a (1, 1) Abrikosov vortex or a (1, −1) PDW dislocation. At a vortex unbinding transition, the lowest-energy vortices will proliferate, leading to a phase that no longer has PDW order but has vestigial order in one of the induced order parameters. In the case that the (1, 1) Abrikosov vortices proliferate (these can be the lowest-energy vortices due to the presence of the vector potential), the resultant phase has only CDW order with a wavevector twice the PDW wavevector (5, 24). In the case that (1, −1) PDW dislocations proliferate, the resultant phase will be a charge-4*e* superconductor (10, 17). As discussed in Section 5.2, this case is particularly relevant in the context of cold atoms because of rotational symmetry.

2.2. Coupling of PDW to Uniform Superconducting Order

The interpretation of a key cuprate experimental result (14) in the context of PDW order requires an understanding of the coexistence of PDW order with usual SC *d*-wave order (Δ_d). Here, we present the simplest coexistence term that allows this to be addressed in zero magnetic field (an

extension to finite field will be discussed later). In zero field, the lowest-order coupling term is given by

$$\mathcal{H}_c = \beta_{c1} \sum_i |\Delta_d|^2 |\Delta_{\mathbf{P}_i}|^2 + \beta_{c2} [{\Delta_d}^2 (\Delta_{\mathbf{P}_x} \Delta_{-\mathbf{P}_x} + \Delta_{\mathbf{P}_y} \Delta_{-\mathbf{P}_y})^* + ({\Delta_d}^2)^* (\Delta_{\mathbf{P}_x} \Delta_{-\mathbf{P}_x} + \Delta_{\mathbf{P}_y} \Delta_{-\mathbf{P}_y})]. \quad 6.$$

A key feature of this coupling is that the β_{c2} term can always be made negative by the correct choice of the relative phases between the PDW and *d*-wave orders. This has two consequences. The first is that this coupling prefers the unidirectional (LO) or bidirectional-I PDW states. The second relates to the observation that coexisting PDW and uniform *d*-wave orders imply the appearance of either CDW $\rho_{\mathbf{P}}$ or MDW $M^z_{\mathbf{P}}$ order at the same momentum as the PDW order. Whether it is CDW or MDW order depends upon the sign of the coefficient β_{c2}; if this coefficient is positive, then MDW appears, if it is negative then CDW order appears. Note that the coupling term β_{c2} locks the phase of the uniform Δ_d order to the unidirectional (LO) and bidirectional PDW phases, and consequently, half-flux quantum vortices will no longer exist. Even if in the ground state Δ_d and $\Delta_{\mathbf{P}}$ do not coexist owing to their competition, it is still possible that they coexist near vortices of either order, where the ground state order parameter is locally suppressed. We refer the reader to Section 3.2 for a review of recent experimental evidence of PDWs near SC vortex halos.

There are two further topics that are not discussed here but deserve some attention. The first is the phenomenological response of the PDW order to static impurities, and the second is the consequence of commensurate PDW order. Nonmagnetic impurities do not couple directly to the PDW order but couple indirectly to the PDW through the induced CDW order (6, 20). The primary consequence of this is that for weak disorder, one expects a destruction of the PDW order because the induced CDW order will be disordered on the Imry–Ma length scale (thereby removing the PDW periodicity on long scales), resulting in vestigial nematic order (25) and charge-4*e* SC order Δ_{4e} (20). In addition, disorder can locally nucleate induced orders that do not generically appear in the PDW ground state of interest (26). In contrast to the above considerations for incommensurate PDW order, in a PDW commensurate with the lattice potential, the latter gaps out the PDW phonons (the $\phi_1 - \phi_2$ mode), thereby precluding half-vortex defects (5).

2.3. Bogoliubov Spectrum of a PDW

Next, we review some properties of the momentum-space Bogoliubov spectrum associated with a PDW and point out a number of features that make it distinct from uniform pairing. As an illustration, we initially discuss what happens to the cuprate band structure if we impose a unidirectional PDW order with $\Delta_{\mathbf{P}_x}, \Delta_{-\mathbf{P}_x}$ on it.

In **Figure 2**, we pair electrons with momenta $\mathbf{p}$ and $2\mathbf{K}-\mathbf{p}$ to form a PDW with momentum $\mathbf{P}_x = 2\mathbf{K}$ and do similarly for $-\mathbf{P}_x$. In this figure, $\mathbf{K}$ was chosen to be at the Fermi surface, but the features we discuss will be similar if $\mathbf{K}$ moves away from the Fermi surface. **Figure 3** shows a cut of the spectrum at $k_y = \pi$, and the solid black line shows the electron band $\epsilon(\mathbf{k}_x)$. We illustrate the formation of the Bogoliubov spectrum with the usual semiconductor representation where the dashed line represents the hole spectrum $-\epsilon(-\mathbf{k}_x + \mathbf{P}_x)$. The hybridization of the two bands form the blue, green, and red bands. We can estimate the weight of these bands in a photoemission experiment by tracking how much of the original solid black band is admixed. For example, the red band is made up mainly of hole bands and will be almost invisible in angle-resolved photoemission spectroscopy (ARPES). The first thing to note is that unlike the uniform

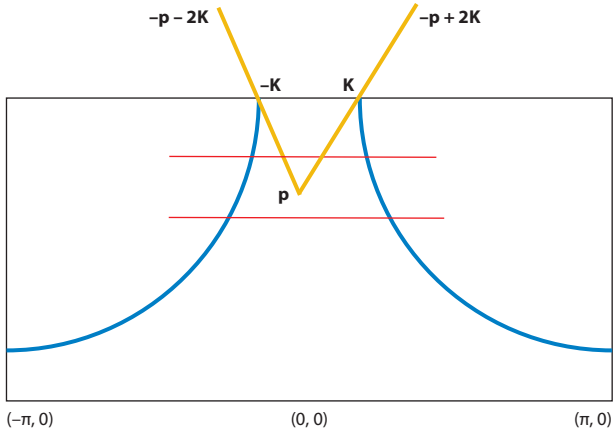

Figure 2

A sketch of the top half of the Brillouin zone for the cuprates with the Fermi surface shown in blue. Pairing of the electrons as indicated form PDW's with momenta $\pm 2\mathbf{K}$ after Umklapp. Figure adapted from Reference 7.

superconductors, the spectrum is not particle–hole symmetric. This is due to the shift of the hole band by $\mathbf{P}_x$. An immediate consequence of this is that the top of the green band does not line up with the Fermi momentum k_F. **Figure 4** shows several scans for different k_y in an experiment performed in Bi-2201 (27). This material is unique in that there is a quite clear onset of the pseudogap

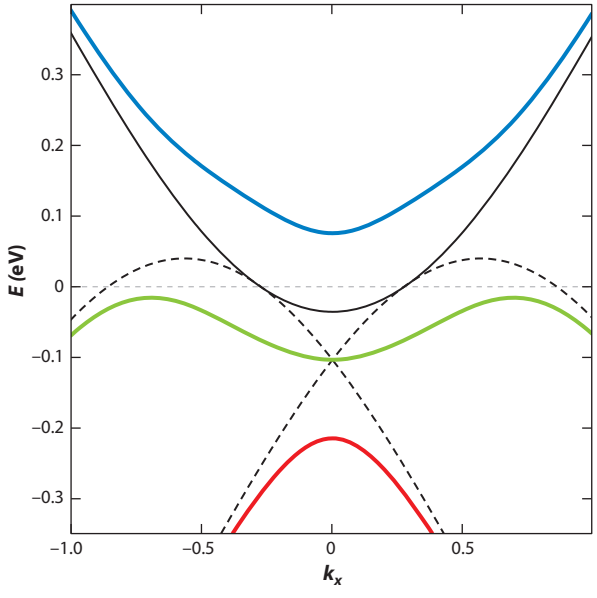

Figure 3

A semiconductor picture of the formation of the Bogoliubov band as a function of k_x for $k_y = \pi$. The solid black line is the original electron dispersion. Dashed lines are the hole bands. Note the shift by the PDW momenta by $\pm\mathbf{P}_x$. The blue, green, and red lines are the resulting hybridized Bogoliubov bands. Figure adapted from Reference 7.

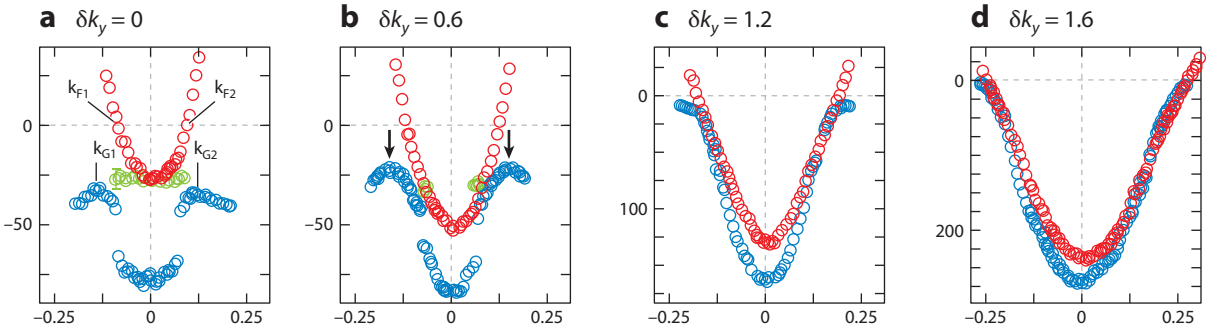

Figure 4

Plots of the ARPES spectra as a function of k_x for several k_y measured from π. The red data points are taken in the high-temperature metallic state. The blue data points are in the pseudogap phase, and the green data points represent additional features that appeared below the superconducting T_c. Abbreviation: ARPES, angle-resolved photoemission spectroscopy. Figure adapted from Reference 7.

at about 140 K while the SC T_c is rather low, so that the spectrum can be mapped out over a wide temperature range covering the high-temperature metallic phase, the pseudogap phase, and the SC phase. An important point noticed by the experimentalists is that in the scan for $k_y = \pi$, the top of the low-temperature band marked by K_G does not line up with the Fermi momentum K_F observed at higher temperature. This was used as an argument against a fluctuating pairing phase as the origin of the pseudogap, but now we see that this objection does not apply to the PDW. Nevertheless, it is worth noting that upon averaging over k space to compute the spectrum that is observed by scanning tunneling spectroscopy (STS) experiments, an approximate particle–hole symmetry can be restored.

A second important observation is that the PDW spectrum naturally has lines of gapless excitations in two dimensions. This is in contrast with the uniform superconductor that can only have nodal points in two dimensions. Although these lines of zeros form closed contours, ARPES is dominated by the electron-like segments that resemble lines of zero crossing. This is commonly referred to as Fermi arc and was first discovered by ARPES experiments in the pseudogap regime. The existence of these arc-like features in the PDW spectrum was pointed out by Baruch & Orgad (28) and Berg et al. (6). Here, we explain how it comes about. Returning to **Figure 3**, imagine gradually moving away from $k_y = \pi$, following the scans indicated by the horizontal lines in **Figure 2**. The black line in **Figure 3** will move down in energy, but the dashed line will move up. Upon hybridization, the top of the green line moves up in energy and eventually crosses zero, resulting in a gapless excitation. With further decrease of k_y from π, these crossings continue and form a closed contour of zero crossings. Most of the electron spectral weight lies on the crossing for k_x closer to the origin. This results in the Fermi arc shown in **Figure 5**, with the back side of the closed loop having almost no weight and being invisible. Here, the arc has been symmetrized assuming the coexistence of PDWs along both the $\mathbf{P}_x$ and $\mathbf{P}_y$ directions.

Finally, let us look at how the zero crossings appear at the ends of the Fermi arc. From our discussion above, it is clear that in the PDW spectrum the zero crossing is formed by an occupied band moving up in energy to meet the Fermi level. This is also what is seen experimentally in **Figure 4** Another candidate for the pseudogap is a CDW at momentum $\mathbf{Q}$. Although this can certainly open a gap at the antinode near $(0, \pi)$, the gap sits at a fixed momentum k_x and as k_y moves away from π, the occupied states only move to lower energy and remain occupied. Therefore, the only way a Fermi arc of gapless excitations can form is for an unoccupied state to move down in energy. This contrasting behavior between a PDW- and CDW-driven antinodal gap and Fermi

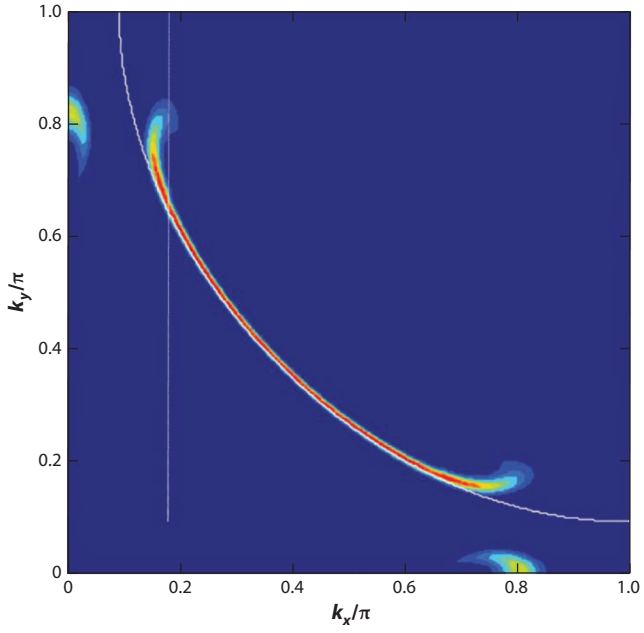

Figure 5

A picture of the Fermi arc of gapless excitations in the PDW state. Figure adapted from Reference 7.

arc was emphasized in References 6 and 7. We also point out that if the PDW is bidirectional and the effect of a composite bidirectional CDW of the type discussed in the last section is added, the Fermi arcs can be connected by the CDW's momenta to form electron-like closed Fermi pockets (7, 13). This mechanism to produce an electron pocket that can explain what is seen in quantum oscillations was first proposed by Harrison & Sebastian (29). The advantage of the PDW picture is that the hole pockets that remain near the antinodes are automatically gapped out. Similar features in the Bogoliubov spectrum were obtained with a different version of the PDW state (30), indicating the robustness of the PDW interpretation of the ARPES spectra. A recent paper studied the spectrum of the PDW in a t-t'-J model, using the self-consistent Gutzwiller approximation, and reached similar conclusions (31).

In summary, the Bogoliubov spectrum associated with the PDW has several features that stand in strong contrast to our intuition based on that of the uniform superconductor. These include the lack of particle–hole symmetry in the spectrum and nodal lines (surfaces) in two (three) dimensions. In the context of cuprate superconductors, many of these features are consistent with ARPES results on Bi-2201, which are very difficult to explain based on CDW, fluctuating d-wave SC, or other conventional pictures (27).

3. CUPRATES

3.1. $La_{2-x}Ba_xCuO_4$ and Related Cuprates

The phase diagram of $La_{2-x}Ba_xCuO_4$ (LBCO), shown in **Figure 6*a***, has an anomalous dip in the bulk SC T_c at $x = 1/8$ (32), which is correlated with the appearance of charge and spin stripe orders, as detected by neutron and X-ray diffraction on single crystals (33, 34). Pinning of the stripes to the lattice is enabled by structural distortion within the CuO_2 layers, such that there is a

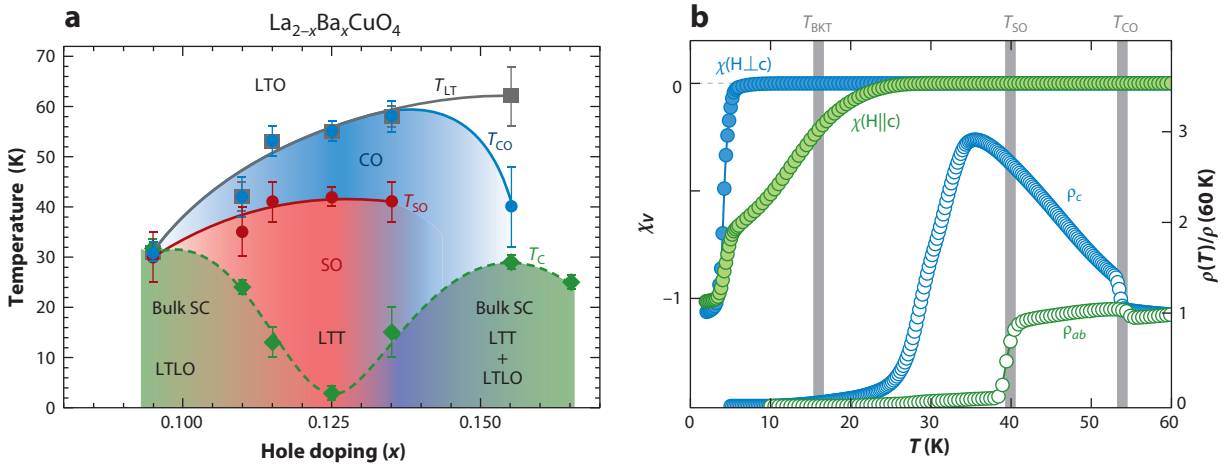

Figure 6

(*a*) Phase diagram for $La_{2-x}Ba_xCuO_4$, indicating CO below T_{co} (limited by the structural transition at T_{LT}), SO below T_{so}, and bulk superconductivity (34). (*b*) Zero-field-cooled volume susceptibility (*left axis*, *filled symbols*) measured with a field of 2 G oriented parallel to the *c* axis (probing in-plane screening) and perpendicular to *c* (probing interlayer screening). In-plane resistivity, ρ_{ab}, and *c*-axis resistivity, ρ_c, (*open symbols*, *right axis*), in $La_{2-x}Ba_xCuO_4$ with $x = 1/8$. Abbreviations: CO, charge order; LTLO, low-temperature less orthorhombic; LTO, low-temperature orthorhombic; LTT, low-temperature tetragonal; SC, superconducting; SO, spin order. Replotted with data from References 38 and 39.

preferred axis along one of the Cu-O directions that rotates by 90° from one layer to the next (35, 36). The relevant distortion appears below a structural phase transition labeled T_{LT} in the figure.

For LBCO with $x = 1/8$, careful measurements of the resistivity within the planes, ρ_{ab}, and perpendicular to the planes, ρ_c, revealed a surprising anisotropy (37, 38). As shown in **Figure 6*b***, cooling below the spin ordering temperature, T_{so}, leads to a drop in ρ_{ab} by an order of magnitude. In contrast, ρ_c continues to rise through T_{so}, eventually turning down at a lower temperature. The drop in ρ_{ab} at ∼40 K appears to correspond to the onset of 2D SC correlations within the CuO_2 layers, as confirmed by measurements of anisotropic diamagnetism (38). Below the transition, ρ_{ab} continues to decrease, extrapolating to zero at $T_{BKT} = 16$ K, where nonlinear transport is observed (37), consistent with a Berezinskii–Kosterlitz–Thouless transition (21, 22); ρ_c remains finite down to ∼10 K, while bulk susceptibility indicates a bulk SC transition at ∼5 K.

Related behavior is observed in rare-earth-doped $La_{2-x}Sr_xCuO_4$, such as $La_{1.6-x}Nd_{0.4}Sr_xCuO_4$ (LNSCO) (40), associated with the same low-temperature structural phase as in LBCO. In particular, a study of the SC state via the *c*-axis optical reflectivity, measured as a function of Nd concentration (which controls the structural phase and the degree of stripe order), demonstrated a sharp decrease in interlayer Josephson coupling corresponding to the rise of stripe order (41). [At low enough frequency, the layers behave as a coherent superconductor, resulting in a reflectivity of unity. At the frequency of the Josephson plasma resonance (JPR), the interlayer coherence breaks down, and charge oscillates between the layers; the reflectivity drops below the normal-state response before recovering at higher frequency (42).] The JPR results on LNSCO, and the studies of LBCO, motivated proposals that PDW order associated with stripes would cause a cancellation of the interlayer Josephson coupling, which is consistent with the observation of 2D superconductivity (3, 4).

Somewhat weaker charge-stripe (43, 44) and spin-stripe (45, 46) order is found in $La_{2-x}Sr_xCuO_4$ with $x \sim 0.12$ in zero field. For $x = 0.10$, it has been observed that applying a

c-axis magnetic field induces spin stripe order (47). Measurements of *c*-axis reflectivity on a similar sample indicate that the field causes a rapid decrease in the coherent interlayer coupling (48). Similar behavior is found in LBCO $x = 0.095$ (49), where superconductivity in the decoupled planes survives to at least 35 T (50). Evidence for bilayer decoupling has recently been reported for $La_{2-x}Ca_{1+x}Cu_2O_6$ (51). The field-induced decoupling is similar to the behavior found in LBCO $x = 0.125$, suggesting that PDW order is present in these samples and that it is less sensitive to magnetic field than is the uniform *d*-wave order.

The loss of coherent coupling between SC layers can be explained by the presence of PDW order, but what do other experiments tell us? The SC gap for PDW order is predicted, in weak-coupling analysis (28), to be large in the antinodal regions of reciprocal space, but zero along finite arcs centered on the *d*-wave nodal points. The gap structure can be tested by ARPES. Such measurements on LBCO $x = 1/8$ do show the antinodal gap, but they also suggest a *d*-wave-like dispersion near the nodal region (52, 53). At the node, however, the spectral function is broad in energy and shifted to ∼20 meV below the chemical potential, similar to a recent observation of a nodal gap in $La_{2-x}Sr_xCuO_4$ with $x = 0.08$ (54). Mean-field calculations of the PDW state that take account of the spin stripe order predict such a gap (55). Although there remains a large degree of uncertainty concerning its interpretation, the ARPES data should not be ignored and will receive further discussion in Section 6.

One picture of the PDW state involves SC stripes that are phase locked by Josephson coupling. That suggests that optical reflectivity measurements with the polarization in-plane but perpendicular to the stripes might yield a response similar to the JPR behavior found in *c*-axis reflectivity. Indeed, such behavior has been observed for LBCO $x = 0.125$, with reflectivity approaching one at low frequency and crossing below the normal-state response above 20 meV, for temperatures of 40 K and below (56). Another test is to apply a *c*-axis magnetic field strong enough to destroy the interstripe Josephson coupling. Such an experiment on LBCO $x = 0.125$ finds that, for $T < 1$ K, fields above 30 T are required to eliminate all 2D coherence, resulting in a highly resistive metallic state with approximate particle–hole symmetry, which is consistent with pair correlations surviving in decoupled charge stripes (57).

The cancellation of the Josephson coupling for PDW orders that are orthogonal in adjacent layers applies for linear interactions. If one can drive large ac currents, then it may be possible to induce a nonlinear coupling. Cavalleri's group has demonstrated this on LBCO with *x* slightly away from 1/8. For $x = 0.115$, the JPR is at a frequency too low to detect; nevertheless, use of a high-intensity terahertz beam generates a JPR response at the third harmonic, even at temperatures far above the bulk T_c (but below the charge-ordering temperature) (58). This experiment provides intriguing evidence for the PDW state.

One of the most distinctive features of the PDW state is the spatial variation of the order parameter between stripes in the same and adjacent planes. The resulting phase structure in turn suggests several approaches for exploring this exotic phase based on probing the nature of quasiparticle and Josephson tunneling into a PDW material. Several such measurements have been carried out that exhibit evidence for the predicted PDW phase.

Scanning tunneling microscopy (STM) on $La_{2-x}Sr_xCuO_4$ $x = 0.12$ with the tunneling current along the *c* axis revealed an unexpected zero-bias anomaly (59). Subsequent calculations in a *t–J* model presented an explanation for this observation from a PDW state exhibiting antiphase domains (60). Additional experiments revealed an anisotropic spatial modulation of the zero-bias peak consistent with this model (61).

For a stripe-ordered cuprate such as LBCO, where the interlayer Josephson coupling is frustrated by the orthogonal stripe orientation in neighboring layers (**Figure 7*a***), a proposed test is

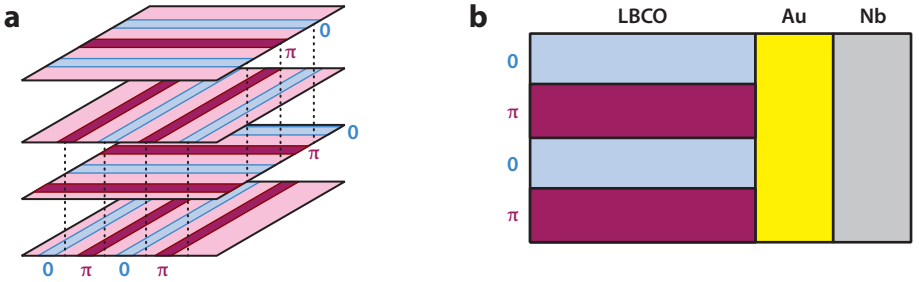

Figure 7

(*a*) The predicted modulation of the phase of the charge stripes in the PDW state. This can be probed by measuring (*b*) the current-phase relation of a Josephson junction fabricated between the crystal (LBCO, $La_{2-x}Ba_xCuO_4$) and a conventional superconductor (Nb) using an Au tunneling barrier.

to reduce the cancellation by applying a magnetic field parallel to the planes; when oriented at 45° to the stripes, the field partially compensates for the momentum mismatch between the layers, causing an enhancement of the Josephson tunneling (62). A test of this type has been done through transport measurements at low temperature and high magnetic field on single crystals of Eu- and Nd-doped $La_{2-x}Sr_xCuO_4$ (63). In a highly dissipative regime with evidence for in-plane SC correlations, the ratio of the *c* axis to the in-plane resistivity decreased as the in-plane field was increased, which is consistent with the predicted scenario.

An even more direct test of the PDW state is to probe the Josephson current-phase relation (CPR) of junctions between the candidate crystal and a conventional superconductor. In the presence of a PDW state, the rapid spatially modulated sign changes in the Josephson coupling will suppress the first-order Josephson coupling and manifest itself as a significant $\sin(2\phi)$ harmonic in the CPR of a junction containing LBCO (see **Figure 7*b***). This phenomenon has been predicted and observed in other junctions with spatially alternating critical current density (64–67). Additionally, we expect the fraction of Josephson current exhibiting a $\sin(2\phi)$ CPR to increase with temperature as the interlayer Josephson coupling and conventional 3D superconductivity are suppressed within LBCO, giving way to an increasing proportion of spatially varying 2D superconductivity within the CuO_2 planes (4).

This experiment has recently been carried out by the Van Harlingen group in Urbana on crystals from Genda Gu at Brookhaven (68). Using both dc Josephson interferometry and anisotropic SQUID measurement techniques, they compared the CPR of $La_{2-x}Ba_xCuO_4$-Au-Nb Josephson junctions for $x = 0.155$ where the T_c is maximum and at $x = 0.125$. As shown in **Figure 8**, at $x = 0.155$, the CPR is nearly sinusoidal, with a nearly negligible $\sin(2\phi)$ component. However, at $x = 0.125$, the nonsinusoidal shape of the CPR arising from the onset of a $\sin(2\phi)$ component is apparent. The expected temperature dependence shown in **Figure 8** was observed. By using junctions fabricated straddling the corner of the crystal, it was also demonstrated that the order parameter symmetry of the crystal remains $d_{x^2-y^2}$ in the region where the T_c is suppressed and the PDW state is present.

3.2. $Bi_2Sr_2CaCu_2O_{8+\delta}$: Vortex Halos and Josephson Microscopy

In this subsection we describe spectroscopic imaging scanning tunneling microscopy (SISTM) and scanned Josephson tunneling microscopy (SJTM) studies of PDW states in the high-T_c superconductor $Bi_2Sr_2CaCu_2O_{8+\delta}$.

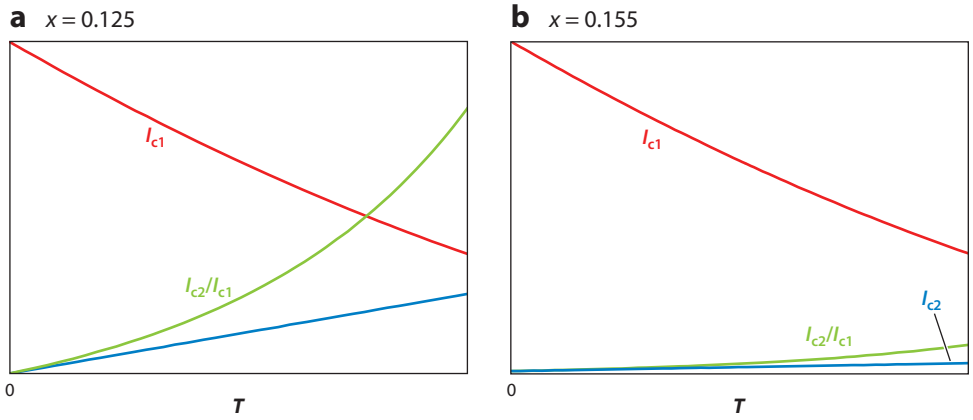

Figure 8

Expected experimental signatures of the PDW state in the current-phase relation of Josephson junctions between $La_{2-x}Ba_xCO_4$ and a conventional superconductor. (*a*) At $x = 0.125$ in the PDW regime, with increasing temperature as the first-order Josephson effect decreases, we expect a growing $\sin(2\phi)$ component of the CPR arising from the phase modulation and a corresponding increase in the ratio of the $\sin(2\phi)$ to $\sin\phi$ component. In contrast, (*b*) at $x = 0.155$ near the maximum T_c, the $\sin(2\phi)$ and its ratio to the $\sin\phi$ component should be very small. Abbreviations: CPR, current-phase relation; FFT, fast Fourier transform.

3.2.1. Spectroscopic imaging and Josephson scanning tunneling microscopy. SISTM (69) has become a key technique for determining electronic structure of quantum materials. At the surface of each sample, the tip-sample differential conductance for single-electron tunneling, $\frac{dI}{dV}\big|_{\mathbf{r},V} \equiv g(\boldsymbol{r}, E)$, is measured versus voltage $V = \frac{E}{e}$ and location $\mathbf{r} = (x, y)$. The resultant array of $g(\mathbf{r}, E)$ images is related to the density of electronic states $N(\mathbf{r}, E)$ as

$$N(\mathbf{r}, E) \propto \frac{g(\mathbf{r}, E)}{\int^{eV_S} g(\mathbf{r})\mathrm{d}E}, \qquad 7.$$

where V_S is a fixed but arbitrary voltage used to establish each tunnel junction. SJTM is a quite different technique in which the magnitude of maximum Cooper-pair tunneling current from an SC tip, $|I_c(\mathbf{r})|$, is measured versus location $\mathbf{r}$, yielding an image of the density of electron pairs in the superconducting condensate.

3.2.2. Evidence for a PDW in $Bi_2Sr_2CaCu_2O_{8+\delta}$ in a magnetic field. In PDW studies, focus has recently turned to modulations of the density of single-electron states $N(\mathbf{r}, E)$ within the vortex halos (70–73)—regions of suppressed but nonzero superconductivity that surround vortex cores. Whether these modulations stem from a field-induced PDW may be studied using Ginzburg–Landau (GL) analysis. Consider a homogeneous *d*-wave superconductor $\Delta_{SC}(\mathbf{r}) = F_d\ \Delta_{SC}$ (where F_d is a *d*-wave form factor) coexisting with a uniform PDW $\Delta^{\mathbf{P}}_{PDW}(\mathbf{r}) = F_{PDW}\Delta_{\mathbf{P}}\left[\exp(i\mathbf{P}\cdot\mathbf{r}) + \exp(-i\mathbf{P}\cdot\mathbf{r})\right]$ with form factor F_{PDW}. The symmetry-allowed $N(\mathbf{r})$ modulations generated by interactions occur as products of these two order parameters that transform as density-like quantities. Specifically, the product $\Delta_{\mathbf{P}}\Delta^*_{SC} \Rightarrow N(\mathbf{r}) \propto \cos(\mathbf{P}\cdot\mathbf{r})$ results in $N(\mathbf{r})$ modulations at the PDW wavevector $\mathbf{P}$, whereas $\Delta_{\mathbf{P}}\Delta^*_{-\mathbf{P}} \Rightarrow N(\mathbf{r}) \propto \cos(2\mathbf{P}\cdot\mathbf{r})$ produces $N(\mathbf{r})$ modulations occurring at $\mathbf{P}$. Consequently, in the case in which PDW order arises in a halo surrounding a vortex in a *d*-wave superconductor, there should be two sets of $N(\mathbf{r})$ modulations at $\mathbf{P}$ and at $2\mathbf{P}$

within each halo, with those at $2\mathbf{P}$ decaying with distance from the core at twice the rate as those at $\mathbf{P}$ [if $\Delta^{\mathbf{P}}_{\rm PDW} = \Delta^{\mathbf{P}}_{\rm PDW}(|\mathbf{r}| = 0)\ \exp(-|\mathbf{r}|/\epsilon)$] (11–14).

To explore these predictions, single-electron tunneling conductance $g(\mathbf{r}, E)$ was measured by Edkins et al. (14) for $Bi_2Sr_2CaCu_2O_{8+\delta}$ samples ($T_c \sim 88$ K, $p \sim 17\%$) at $T = 2$ K. The $g(\mathbf{r}, E)$ is first measured at zero field and then at magnetic field $B = 8.25$ T, in the identical field of view (FOV) using an identical STM tip. The $g(\mathbf{r}, E, B)$ and $g(\mathbf{r}, E, 0)$ are registered to each other with picometer precision and then subtracted to yield $\delta g(\mathbf{r}, E, B) = g(\mathbf{r}, E, B) - g(\mathbf{r}, E, 0)$. This result is the field-induced perturbation to the density of states $\delta N(\mathbf{r}, E, B) \propto \delta g(\mathbf{r}, E, B)$.

Figure 9*a* shows measured $\delta g(\mathbf{r}, E = 10\,\text{meV}, B)$ exhibiting the classic halo of modulations in the density of Bogoliubov quasiparticles at $\mathbf{q} \approx [(\pm 1/4, 0); (0, \pm 1/4)\frac{2\pi}{a_0}]$. However, for the energy range $25 < |E| < 50$ meV, which is $|E| \approx \Delta_{\rm SC}$, the measured $\delta g(\mathbf{r}, E = 30\,\text{meV}, B)$ shown in **Figure 9*b*** contains distinct modulations within each halo. Fourier analysis yields $\left|\widetilde{\delta g}(\mathbf{q}, 30\,\text{meV})\right|$, as shown in **Figure 9*c***, reveals a set of eight maxima at $\mathbf{q} = [\mathbf{P}_x; \mathbf{P}_y] \approx [(\pm\frac{1}{8}, 0); (0, \pm\frac{1}{8})]2\pi/a_0$, which we label $\mathbf{P}$, and at $\mathbf{q} \approx [(\pm\frac{1}{4}, 0); (0, \pm\frac{1}{4})]2\pi/a_0$, which we label $2\mathbf{P}$. The inset to **Figure 9*c*** shows the measured amplitude $\left|\widetilde{\delta g}(\mathbf{q}, 30\,\text{meV})\right|$ along (1, 0), indicating that the field-induced $N(\mathbf{r}, E)$ modulations occur, with both $\lambda \approx 8a_0$ and $\lambda \approx 4a_0$, along both the (1, 0);(0, 1) directions within every vortex halo. The fitted widths $\delta(\mathbf{P})$ of all $|\mathbf{P}| \approx (1/8)2\pi/a_0$ peaks are close to half that of the $|2\mathbf{P}| \approx 1/4(2\pi/a_0)$ peaks: $\delta(2\mathbf{P}) = 1.8 \pm 0.2)\delta(\mathbf{P})$. These phenomena occur in a particle–hole symmetric manner for $25 < |E| < 45$ meV and exhibit predominantly *s*-symmetry form factor modulations at $\mathbf{P}$ and $2\mathbf{P}$. Finally, measured field-induced energy gap modulations $\delta\Delta(\mathbf{r}) = \Delta(\mathbf{r}, B) - \Delta(\mathbf{r}, 0)$ yield a Fourier transform $\widetilde{\delta\Delta}(\mathbf{q})$ that exhibits energy-gap modulation at $\mathbf{P}$ but not at $2\mathbf{P}$. In the context of Ginzburg–Landau theory (11–14), these data indicate that, in $Bi_2Sr_2CaCu_2O_{8+\delta}$, a field-induced PDW state emerges within the halo region surrounding each quantized vortex core.

3.2.3. Evidence for a PDW in $Bi_2Sr_2CaCu_2O_{8+\delta}$ at zero magnetic field. Atomic-resolution SC STM tips (74) have also been applied for the study of the PDW state in underdoped cuprates, but at $B = 0$. Ideally, if both the tip and sample are SC, with identical SC energy gaps $\Delta(\mathbf{r})$ and quantum phase difference ϕ, a Josephson current $I(\phi) = I_J \sin(\phi)$ of Cooper pairs can ensue. However, for nanometer-scale junctions with normal-state resistance in the gigaohm range, thermal fluctuations will overwhelm stable-phase Josephson tunneling until the submillikelvin temperature range. Instead, phase-diffusion-dominated Josephson tunneling is usually achieved, in which the measured $I(V)$ exhibits a maximum current $I_c \propto I_J^2$ (75). Measuring $|I_c(\mathbf{r})|$ has therefore become the established approach for visualizing the variation of Josephson tunneling (75–78) and thus of superfluid (electron-pair) density $\rho_s(\mathbf{r})$.

In a PDW of the type $\Delta^{\mathbf{P}}_{\rm PDW}(\mathbf{r}) = F_{\rm pdw}\Delta_{\mathbf{P}}(\mathbf{r})\left[\exp(i\mathbf{P}\cdot\mathbf{r}) + \exp(-i\mathbf{P}\cdot\mathbf{r})\right]$, the superfluid density $\rho_s(\mathbf{r})$ modulates spatially. Searches for such phenomena in cuprates required visualizing $|I_c(\mathbf{r})|$ with nanometer resolution, high I_J, low R_N, and low operating temperatures. For the $Bi_2Sr_2CaCu_2O_{8+\delta}$ samples ($T_c = 88$ K, $p = 0.17$) studied by Hamidian et al. (79), the STM operates below 50 mK, and high I_J achieved using an exfoliated nanometer-sized flake of $Bi_2Sr_2CaCu_2O_{8+\delta}$ with spatial resolution ~1 nm adhering to the end of each tungsten STM tip. **Figure 10*a*** shows a typical $|I_c(\mathbf{r})|$ image measured under those conditions, clearly exhibiting periodic modulations in $\rho_s(\mathbf{r})$ along the CuO_2 axes (1, 0);(0, 1). **Figure 10*b*** shows $|\tilde{I}_c(\mathbf{q})|$, the magnitude of the Fourier transform of $|I_c(\mathbf{r})|$, indicating that the wavevectors of $\rho_s(\mathbf{r})$ modulations in $Bi_2Sr_2CaCu_2O_{8+\delta}$ are at $\mathbf{q} = (0.25 \pm 0.02, 0)2\pi/a_0$; $(0, 0.25 \pm 0.02)2\pi/a_0$.

Single-electron tunneling SISTM studies on equivalent $Bi_2Sr_2CaCu_2O_{8+\delta}$ crystals reveal intense electronic structure modulations (80–82) that are locally commensurate (83, 84) and unidirectional (82, 85), exhibit $4a_0$ periodicity (83, 84) with a *d*-symmetry form factor (85, 86), and

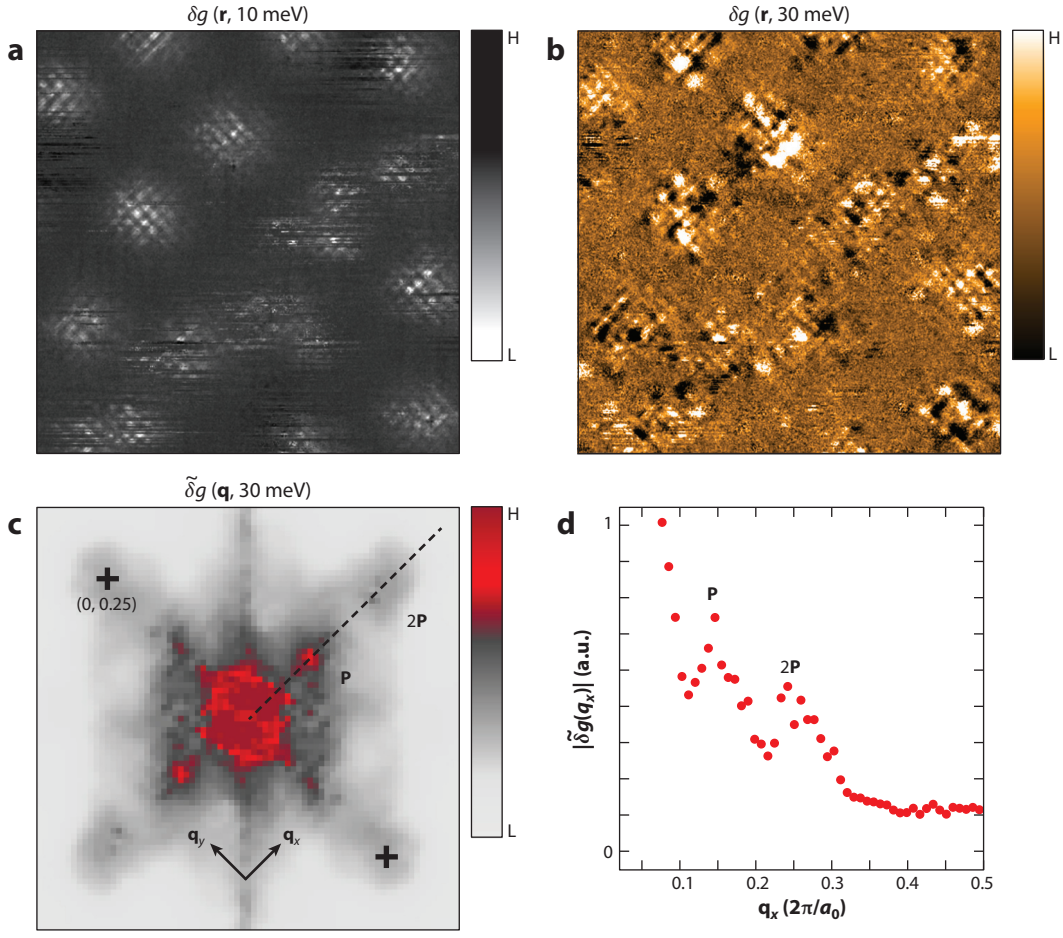

Figure 9

(*a*) Measured $\delta g(\mathbf{r}, E, B) = g(\mathbf{r}, E = 10\,\text{meV}, B = 8.25\,\text{T}) - g(\mathbf{r}, E = 10\,\text{meV}, B = 0\,\text{T})$ in a 58 nm × 58 nm FOV, showing typical examples of the low-energy Bogoliubov quasiparticle modulations within halo regions surrounding four vortex cores in $Bi_2Sr_2CaCu_2O_{8+\delta}$. (*b*) Measured field-induced modulations $\delta g(\mathbf{r}, E = 30\,\text{meV}, B) = g(\mathbf{r}, E = 30\,\text{meV}, B = 8.25\,\text{T}) - g(\mathbf{r}, E = 30\,\text{meV}, B = 0\,\text{T})$ in the same 58 nm × 58 nm FOV. Although the vortex halos are clearly seen to occur at exactly the same locations as in panel *a*, the modulations therein are radically different. (*c*) Amplitude Fourier transform $\left|\widetilde{\delta g}(\mathbf{q}, 30\,\text{meV})\right|$ (square root of power spectral density) of $\delta g(\mathbf{r}, E = 30\,\text{meV}, B)$ data in panel *b*. The $\mathbf{q} \approx [(\pm\frac{1}{4}, 0); (0, \pm\frac{1}{4})]2\pi/a_0$ points are indicated by black crosses. Four sharp maxima, indicated by $\mathbf{P}$, occur at $\mathbf{q} = [\mathbf{P}_x; \mathbf{P}_y] \approx [(\pm\frac{1}{8}, 0); (0, \pm\frac{1}{8})]2\pi/a_0$, whereas four broader maxima, indicated by $2\mathbf{P}$ occur at $\mathbf{q} \approx [(\pm\frac{1}{4}, 0); (0, \pm\frac{1}{4})]2\pi/a_0$. (*d*) Measured $\left|\widetilde{\delta g}(\mathbf{q}, 30\,\text{meV})\right|$ along (0, 0)–(1/2, 0) showing the two distinct maxima in the field-induced $N(\mathbf{r})$ modulations, occurring at $\mathbf{P} = 0.117 \pm 0.01$ and $2\mathbf{P} = 0.231 \pm 0.01$. Abbreviations: H, high; L, low. Figure from Reference 14 with permission.

are concentrated at particle–hole symmetric energies $|E| \approx \Delta_1$, where Δ_1 is the pseudogap energy scale (69, 81, 82, 85).

At values of p where simultaneous data exist, the wavelengths of these modulations are indistinguishable from those in $|I_c(\mathbf{r})|$ (e.g., **Figure 10*b***) within joint uncertainty. Although this is consistent with a composite PDW order formed out of a CDW with the same wavevector and the uniform *d*-wave superconductivity, whether the order parameter of the fundamental state underpinning these single-electron signatures is a CDW or a PDW remains to be determined. The

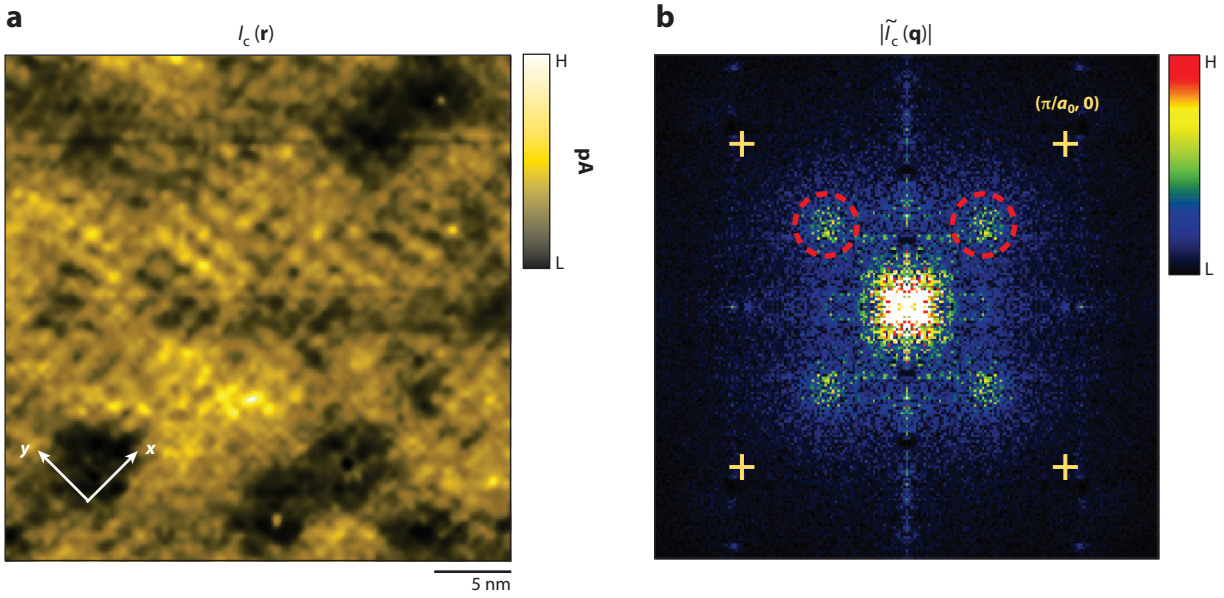

Figure 10

(*a*) Typical $I_c(\mathbf{r})$ image from $Bi_2Sr_2CaCu_2O_{8+\delta}$ at $p = 0.17\%$. The $I_c(\mathbf{r})$ modulations are parallel to the CuO_2 directions [structural supermodulation-induced $I_c(\mathbf{r})$ modulations along the (1, 1) directions are removed]. (*b*) $|(I_c(\mathbf{q})|$, the Fourier transform of $I_c(\mathbf{r})$ [crosses at $\mathbf{q} = (\pi/a_0, 0)$; $(0, \pi/a_0)$]. Maxima from $I_c(\mathbf{r})$ modulations (*dashed red circles*) occur at $\mathbf{q} = (0.25, 0)2\pi/a_0$; $(0, 0.25)2\pi/a_0$. Abbreviations: H, high; L, low. Figure adapted from Reference 79.

relationship of the $|I_c(\mathbf{r})|$ modulations observed at zero magnetic field to the PDW in vortex halos also remains unclear, as it is yet to be established whether the $\lambda \approx 4a_0$ $I_c(\mathbf{r})$ modulations are consistent with an underlying $\lambda \approx 8a_0$ PDW as expected. Nevertheless, the $|I_c(\mathbf{r})|$ imaging data (e.g., **Figure 10**) provide strong direct evidence for the existence of a PDW coexisting with a robust homogeneous Cooper-pair condensate in underdoped $Bi_2Sr_2CaCu_2O_{8+\delta}$.

4. OTHER SYSTEMS

4.1. Organics, Fe-Based Superconductors, and Heavy Fermion Materials

A variety of materials have been argued to be candidates for the originally proposed FFLO state, in which a Zeeman field shifts the energy of the up-spin and down-spin partners of the Cooper pairs in opposite directions, such that it becomes energetically beneficial to create Cooper pairs with finite momentum. The materials discussed in this section have been reviewed previously (87–89), so here we highlight the main results and refer to these reviews for more detail.

The most compelling case for realizing the original FFLO-like PDW superconductor (1, 2) is in organic materials. A detailed overview of the experimental evidence for this in quasi-2D organic materials with in-plane magnetic fields is given in Reference 87. Organic materials have proven to be ideal for realizing the FFLO-like PDW phase for three reasons: They are quasi-2D, suppressing the creation of vortices and allowing the high fields needed to create FFLO-like PDW states to be reached; they are clean with mean free paths typically a factor of 10–100 greater than the SC coherence length; and they have weak spin-orbit coupling. The primary evidence for the existence of the FFLO state is largely of three types: the observation of the characteristic upturn of the upper

critical field at low temperatures; the observation of two high-field phase transitions at low temperatures; and the observation of an inhomogeneous magnetic field distribution consistent with that expected for an FFLO-like phase. κ-(BEDT-TTF)$_2$Cu(NCS)$_2$ presents the strongest case in which magnetic torque measurements suggest (*a*) a first-order transition line at high fields inside the SC state (90, 91), specific heat measurements observing the same first-order transition (92, 93), NMR measurements consistent with the observation of spin-polarized quasiparticles localized near the spatial nodes of the FFLO order parameters (94, 95), and evidence of multiple phase transitions in rf-penetration depth measurements (96). Among the quasi-2D organics there is also evidence for an FFLO-like PDW state in λ-(BETS)$_2$GaCl$_4$ (97, 98) and β''-(ET)$_2$SF$_5$CH$_2$CF$_2$SO$_3$ (99, 100). In addition, resistivity measurements observe an upper critical field and field anisotropy behavior consistent with an FFLO-like PDW state in the quasi-1D organic (TMTSF)$_2$ClO$_4$ (101).

Fe-based superconductors represent a likely class of materials that can realize an FFLO state because of their high upper critical fields (102). To date, experimental evidence has been found for an FFLO-like PDW state in KFe$_2$As$_2$ (103) in which magnetic torque and specific heat measurements observe two SC transitions at high fields and observe a characteristic upturn of the upper critical field at low temperatures.

Finally, there were reports that FFLO phases also appear in the heavy fermions superconductors UPd$_2$Al$_3$ (104, 105), CeRu$_2$ (105, 106), and CeCoIn$_5$ (107, 108). However, the phase transition attributed to the FFLO-like PDW phase in both UPd$_2$Al$_3$ and CeRu$_2$ has been argued to be a consequence of a vortex-related transition (88). The case for CeCoIn$_5$ is much more interesting. Subsequent to the original discovery of a new low-temperature, high-field SC phase that was argued to be an FFLO-like PDW phase (107, 108), this phase was found to have spin-density wave (SDW) order (109). This SDW order exists only within the SC state. Due to the coexistence of usual superconductivity and SDW order, PDW order will also generically exist (16), making it difficult to identify a primary order parameter. This has led to many proposals that are still being experimentally untangled (89).

4.2. PDW in Degenerate Atomic Gases: FFLO

Experimental progress in trapping, cooling, and coherently manipulating Feshbach-resonant atomic gases opened unprecedented opportunities to study degenerate strongly interacting quantum many-body systems in a broad range of previously unexplored regimes (110–114). This has led to a realization of paired fermionic superfluids (115–117) and the associated Bardeen–Cooper–Schrieffer (BCS) to Bose–Einstein condensation (BEC) crossover (118–120).

These neutral atomic systems are particularly well suited to imposing (pseudo-)magnetization, corresponding to the number imbalance $P \equiv (N_\uparrow - N_\downarrow)/N$ in the pairing hyperfine $\uparrow - \downarrow$ species, circumventing challenges of charged electronic superconductors realized in solid state, as discussed in much of this review (121–124). The imbalance and the associated Fermi surface mismatch frustrate the singlet paired state (125–128) driving quantum phase transitions out of the gapped BCS superfluid to a variety of putative ground states and thermodynamic phases (129–134). One of the most interesting is the FFLO finite-momentum paired state (1, 2).

Experiments (121–124) on trapped atomic systems have extensively explored and established the predicted interaction-imbalance phase diagram, illustrated in **Figure 11** (131, 135, 136), dominated by the superfluid to (polarized) FL first-order phase transition, that manifests in phase separation (127, 132, 135). However, outside of one dimension, so far, no signatures of the enigmatic FFLO PDW state (1, 2) have been seen. This is consistent with the narrowness of the FFLO sliver in the predicted phase diagram (131, 135), though much remains to be understood about FFLO's stability beyond mean-field analyses of simplest FFLO states (137, 138).

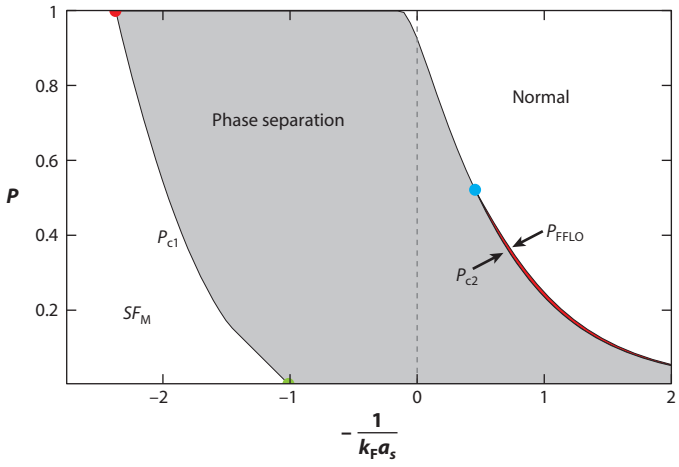

Figure 11

A mean-field zero-temperature phase diagram of an imbalanced Fermi gas, as a function of the inverse scattering length and normalized species imbalance (dimensionless magnetization), $P = (N_\uparrow - N_\downarrow)/N \equiv \Delta N/N$, showing the magnetized (imbalanced) superfluid (SF_M), the FFLO state (approximated as the simplest FF state, confined to a narrow red sliver bounded by P_{FFLO} and P_{c2}) and the imbalanced normal Fermi liquid. Abbreviations: FF, Fulde–Ferrell; FFLO, Fulde–Ferrell–Larkin–Ovchinniko. Data from References 131 and 135.

In contrast, in one dimension (where it is robust and generic at any nonzero imbalance), the FFLO state has been experimentally realized in a two-dimensional array of decoupled one-dimensional traps, generated via a two-dimensional optical periodic potential (139). Although spin-resolved density profiles in these experiments shows consistency with the FFLO interpretation, they still lack the "smoking gun" observation of, e.g., a finite momentum condensate peak in the momentum distribution function, precluded in the thermodynamic limit in one dimension by strong quantum and thermal fluctuations and by the inhomogeneous atomic density special to trapped gases.

Experimental efforts are under way to move toward the quasi-1D limit of coupled tubes, and in fact the 1D–3D crossover signatures have been experimentally demonstrated (140, 141). This is done by reducing the strength of the periodic optical potential, thereby allowing the 1D PDWs of neighboring tubes to lock through intertube coupling. Cooling and equilibration, particularly for pseudospin, remains a challenging experimental problem.

5. MECHANISM

5.1. Evidence of PDWs in Models of Strongly Correlated Systems

Condensates with finite momentum are problematic in conventional BCS theory. In the first place, so long as either time-reversal or inversion symmetry is preserved, the Fermi surface is always perfectly nested for some form of $\mathbf{P} = \mathbf{0}$ pairing; i.e., the SC susceptibility is peaked and logarithmically divergent as $T \to 0$, whereas it remains finite at all nonvanishing $\mathbf{P}$. If the $\mathbf{P} = \mathbf{0}$ divergence is quenched, as it is in any singlet channel by a finite Zeeman field, as recognized by Fulde & Ferrell (2) and Larkin & Ovchinnikov (1), the pair susceptibility can be peaked at a nonzero $\mathbf{P}$, but in that case it remains finite even as $T \to 0$. In the Hartree–Fock approximation, used in BCS theory, lack of nesting leads to a finite critical coupling for the condensate to occur even at zero

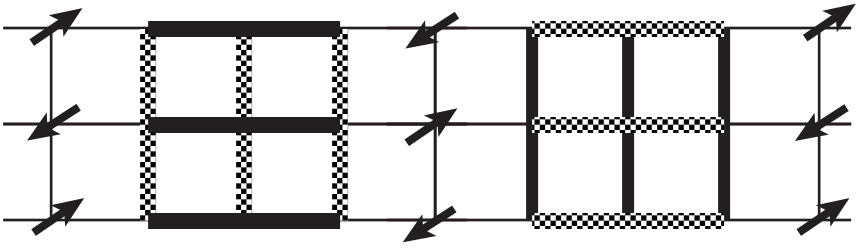

Figure 12

Qualitative picture of the PDW. The local superconducting order parameter is *d*-wave: positive (negative) in the bold (shaded) links, and axes rotate after a half-period. In this example, presumably applicable to $La_{2-x}Ba_xCuO_4$, the PDW is intertwined with spin stripe order. Notice that the charge density has half the period of the PDW order. Figure adapted from Reference 4.

temperature. In the case of FFLO states, the Zeeman coupling to the external magnetic field acts as a small tuning parameter; i.e., the critical coupling can still be parametrically small.

In contrast, for the putative PDW states of high T_c superconductors (HTSC), which occur in the absence of an external Zeeman coupling, no such small tuning parameter exists. Even the naive application of BCS theory to PDW states typically requires a critical coupling of strength comparable with the bandwidth. More importantly, the SC states in these materials, uniform or not, arise in strongly correlated systems whose normal state is a strange metal, a metallic state without well-defined fermionic quasiparticles.

The PDW looks locally like a *d*-wave superconductor. It breaks translation symmetry in such a way that the order parameter changes sign upon translation by half a period (see **Figure 12**). Therefore, it is reasonable to suppose that it is a close competitor of the uniform *d*-wave superconductor under strong-coupling circumstances in which correlation lengths are short and the important physics is correspondingly local. Indeed, in the context of a proposed SO(5) theory of intertwined antiferromagnetic and *d*-wave SC order, it was proposed in 1998 by Zhang (142) that an SO(5) spiral state consisting of alternating stripes of Néel order and *d*-wave SC order—precisely the sort of intertwined PDW and spin stripe shown in **Figure 12**—might arise in some circumstances. A variety of subsequent studies employing variational wave functions have also found such states, starting with the 2002 study by Himeda, Kato & Ogata (3), who used variational Monte Carlo calculations of Gutzwiller-projected wave functions for the ground state of the t-t'-J model. These states are inhomogeneous versions of the doped resonating valence bond (RVB) wave functions widely used as candidate ground states for the t-J model. These early results, as well as later variational and renormalized mean-field studies (60, 143, 144), found three states whose variational ground-state energies are very close: the uniform *d*-wave superconductor, the PDW state, and a striped *d*-wave superconductor. For doping near $x = 1/8$, these variational studies found period 4 states with half-filled stripes. The intertwined nature of the PDW states was also proposed on phenomenological grounds in References 4, 6, and 7.

BCS mean-field methods have also been used to describe PDW phases. Loder and coworkers (55, 145) used BCS mean-field theory for a 2D system with a t-t' band structure widely used in the cuprates and an effective attractive interaction for electrons on nearest-neighboring sites of strength V (assumed to originate from spin fluctuations). Within a BCS-type mean-field theory, these authors find that while in the weak coupling regime the ground state is a uniform *d*-wave superconductor for systems near 1/8 doping, for V larger than a critical value $V_c \gtrsim t$, the preferred pairing state is locally *d*-wave but has a finite momentum, i.e., a PDW, with or without an associated spin stripe state. A subsequent publication by Wårdth & Granath found that V_c is significantly

larger than this estimate (146). These authors proposed a model with an interaction with local attraction and longer-range phase slip pair hopping and found, using a BCS-type theory, that the critical coupling for the PDW state is significantly reduced and typically of the order of the kinetic energy bandwidth (146, 147).

Other microscopic mechanisms have also been proposed and studied within mean-field approaches. Lee proposed an Amperean pairing mechanism (7), due to local spin current fluctuations in an RVB-type state (148), and showed (in mean-field theory) that it favors a PDW. Soto-Garrido & Fradkin (149) studied the SC condensates arising in the vicinity of a (Pomeranchuk) instability in the quadrupolar spin triplet channel of an FL (150), and found that the PDW competes with a spin triplet p and a spin singlet d-wave SC states. Soto-Garrido and coworkers (151) used a quasi-1D approach based on a model of stripe phases (152) and found PDW states.

At present, the only model that has been definitively shown to have a PDW state is in a model of strongly correlated systems in one dimension known as the Kondo–Heisenberg chain. This model consists of a 1D system of mobile electrons, a Luttinger liquid, coupled by a local Kondo exchange interaction J_K to a spin-1/2 quantum Heisenberg antiferromagnetic chain with exchange coupling J_H. Models of this type have been studied for a long time in the context of the physics of heavy-fermion superconductors. Bosonization and density-matrix renormalization group (DMRG) studies by Sikkema, Affleck & White revealed that for $J_H \gtrsim J_K$ this system has a spin gap (153), which was subsequently interpreted as an exotic η-pairing SC state (154, 155). Specifically, the dominant long-range (power-law) correlations involve an oscillatory charge-2e order parameter, but it is a composite order in the sense that it cannot be simply expressed as a product of two electron creation operators. Berg, Fradkin & Kivelson (156) reexamined this system by DMRG and showed that it is indeed a PDW state, albeit an exotic one. Specifically, on open chains with different boundary conditions, they showed that in this state all the fermion bilinear operators decay exponentially with distance. Only order parameters that are composite operators of the Luttinger liquid and the spin chain have (quasi) long-range order, as suggested by the bosonization studies. For instance, the PDW order parameter is realized as the scalar product of the Néel order parameter of the spin chain with the spin triplet superconductor of the Luttinger liquid, and it has quasi-long-range order. [Remarkably, later work showed that this incarnation of the PDW is actually a topological superconductor (157).] Similar behavior was found for the expected charge-4e uniform SC order parameter. Later on, similar results were found for extended generalized Hubbard models on 2-leg ladders at special filling fractions of the bonding band (158).

A real challenge is establishing the existence of a PDW state in two dimensions using unbiased approaches, even numerically. Due to the notorious fermion sign problem, quantum Monte Carlo methods are only useful at relatively high temperatures and have not been able to reach low enough temperatures to see unambiguous signs of d-wave superconductivity in Hubbard models and its generalizations. Nonetheless, down to the lowest temperatures accessible, such calculations always find an SC susceptibility that is peaked at $\mathbf{P} = \mathbf{0}$ (159). However, exact diagonalizations can only deal with systems that are too small to be useful to detect PDW states (even if they were ground states). One option is DMRG simulations on relatively wide ladders, and we discuss these in the next paragraphs. DMRG methods are known to be asymptotically exact matrix-product states (at least for gapped states), whose accuracy can be improved by increasing the bond dimension of the tensors. These approaches are known to generate large enough quantum entanglement to produce most states of interest in one-dimensional systems, including quantum critical states.

Other options include tensor network approaches that, conceptually, are extensions of DMRG to higher dimensions. However, while in 1D it is known that matrix product states are sufficient to

describe most systems of interest, in higher dimensions this is an open question. The current most widely used tensor network approach is PEPS (projected entangled paired states) (160). PEPS and its relative iPEPS (infinite PEPS) consist of a variational ansatz in the form of a tensor network (a matrix product state) with many variational parameters that grow as a power of the bond dimension (the dimension of the tensor), of order $3D^4$, where D is the bond dimension. Unlike conventional variational wavefunctions, which are essentially product states (and hence have only short-range entanglement), iPEPS can describe more complex states with large-scale entanglement. Corboz and coworkers (161) initiated a study of the t-J model as a function of doping. In the most recent study of this type (162) it was found that, for a wide range of parameters J/t and doping δ, the uniform d-wave superconductor, the striped superconductor, and the PDW (called the antiphase stripe state by Corboz et al.), are essentially degenerate. Although this result agrees with the simpler variational wave functions discussed above, in the iPEPS generated states the charge stripes are not half-filled and, in fact, their occupancy varies continuously with J/t. (Were such a PDW state to be relevant in the cuprates, its period would not be particularly pinned to $8a$, even near 1/8 doping, in contrast with experiment in LBCO.) The iPEPS results are highly encouraging for the existence of PDW order. However, we are careful to note that it is currently unclear what biases are implied in this approach, and these results need to be benchmarked against other techniques.

Quite recently, large-scale DMRG simulations of the t-J model on 4-leg ladders in the doping range of 5–12.5% with $t/J = 3$ (and other values as well) (163–165) have been carried out. These authors find strong evidence for d-wave superconductivity (i.e., a sign change of the SC amplitude along two orthogonal directions) and charge-stripe phases with 1/2 a hole per unit cell. These simulations kept a significantly larger number of states in the DMRG than earlier studies. However, although the parameter range examined by these authors is broad and overlaps with those used in the iPEPS simulations discussed above, no evidence for PDW states have (yet) been detected in the DMRG. This result is in apparent contradiction with the iPEPS results, and this discrepancy is quite puzzling. This is a pressing problem, and a deeper understanding of the advantages and limitations of these methods is clearly required. A recent DMRG study of a doped t-J model on a triangular lattice with ring exchange interactions found encouraging evidence of PDW-like SC correlations that change sign as a function of distance, but which fall sufficiently rapidly (at least like r^{-4}) that they do not give rise to a diverging susceptibility as $T \to 0$ (166).

We close this section by noting that PDW states have been studied using methods of holography, the Anti–de Sitter/conformal field theory (AdS-CFT) correspondence. Although it is not clear what microscopic systems can be described with holography, these theories have the clear advantage of describing metallic states without well-defined quasiparticles (167). Several holographic models have been published describing superconductors with striped phases (168) and systems with intertwined SC and PDW orders (169–171).

5.2. Fulde–Ferrell–Larkin–Ovchinnikov State in Degenerate Atomic Gases

One context in which an FFLO state has a well-understood microscopic mechanism is a singlet superconductor with pairing frustrated by a magnetic field (1, 2, 172–174). An ideal realization of such a system is a pseudospin imbalanced Feshbach-resonant atomic Fermi gas (121–124), where (in contrast to charged electronic superconductors in solid state) the Zeeman component of the magnetic field and the effective magnetization can be tuned independently of the obscuring orbital field effects, such as vortices. This has rekindled extensive theoretical research (125–128, 131, 132, 134–136, 141, 175) reviewed in References 9 and 114.

5.2.1. Model of a resonant Fermi gas. A neutral fermionic atomic gas is well captured by a microscopic Hamiltonian

$$H = \sum_{\mathbf{k},\sigma} (\epsilon_{\mathrm{k}} - \mu_\sigma) \hat{c}^\dagger_{\mathbf{k}\sigma} \hat{c}_{\mathbf{k}\sigma} + g \sum_{\mathbf{k}\mathbf{k}'\mathbf{q}} \hat{c}^\dagger_{\mathbf{k}\uparrow} \hat{c}^\dagger_{-\mathbf{k}+\mathbf{q}\downarrow} \hat{c}_{-\mathbf{k}'+\mathbf{q}\downarrow} \hat{c}_{\mathbf{k}'\uparrow}, \quad 8.$$

with the single-particle energy $\epsilon_{\mathrm{k}} = \hbar^2 k^2/2m$. The separately conserved number $N_\sigma = (N_\uparrow, N_\downarrow)$ of atomic species (hyperfine states) $\sigma = (\uparrow, \downarrow)$ is imposed by two chemical potentials, $\mu_\sigma = (\mu_\uparrow, \mu_\downarrow)$, or equivalently by the average chemical potential $\mu = \frac{1}{2}(\mu_\uparrow + \mu_\downarrow)$ and the Zeeman field $h = \frac{1}{2}(\mu_\uparrow - \mu_\downarrow)$, which respectively tune the total atom number $N = N_\uparrow + N_\downarrow$ and atom pseudospin imbalance $\Delta N = N_\uparrow - N_\downarrow$.

Key features distinguishing this Fermi system from those familiar electronic ones in solid state contexts (discussed in other parts of this review) are (*a*) the fermions are neutral and thus do not couple to the electromagnetic vector potential; (*b*) the absence of a periodic ionic potential (though an optical lattice can be imposed by an off-resonant interfering laser field) that explicitly breaks rotational and translational spatial symmetries; and (*c*) the resonant nature of the Feshbach interaction, parameterized by a short-range *s*-wave pseudopotential, $g < 0$. The resulting attractive interaction can be computed through an exact T-matrix scattering analysis (112), with g controlling the magnetic-field-tunable (176) 3D scattering length,

$$a_{\mathrm{s}}(g) = \frac{m}{4\pi} \frac{g}{1 + g/g_{\mathrm{c}}}, \quad 9.$$

that diverges above a critical attraction strength, $|g| = g_{\mathrm{c}} \equiv 2\pi^2 d/m$, corresponding to a threshold for a two-atom bound state of size d.

The Zeeman h field–driven Fermi surface mismatch (that, for these neutral fermions can be tuned independently of the orbital field and can also be realized via atomic mass and other dispersion imbalance), energetically penalizes the conventional BCS $-\mathbf{k}$ to $\mathbf{k}$ pairing at weak coupling. However, as noted at the beginning of Section 5.1, a finite momentum $\mathbf{P}$ pairing, $\Delta_{\mathbf{P}} = \sum_{\mathbf{k}} g \langle c_{-\mathbf{k}\downarrow} c_{\mathbf{k}+\mathbf{P}\uparrow} \rangle$ (set by the Fermi surface mismatch) allows for an FFLO ground state, which compromises between a fully paired superconductor and a magnetized FL (1, 2).

The simplest treatment is a mean-field analysis (131, 135) for the PDW order parameter $\Delta(\mathbf{r}) = \sum_{\mathbf{p}} \Delta_{\mathbf{p}} e^{i\mathbf{p}\cdot\mathbf{r}} = g\langle \hat{c}_\downarrow(\mathbf{r}) \hat{c}_\uparrow(\mathbf{r}) \rangle$, generalized to pair-condensation at a set of reciprocal lattice vectors, $\mathbf{p}$, with the amplitudes $\Delta_{\mathbf{p}}$ and $\mathbf{p}$ self-consistently determined by minimizing the ground state energy. This gives a satisfactory qualitative description (quantitatively valid deep in the weakly coupled BCS regime, $k_{\mathrm{F}}|a_{\mathrm{s}}| \ll 1$), as a starting point of more sophisticated large-N_f (177, 178) and ϵ-expansion (179) treatments.

5.2.2. Ginzburg–Landau model and transitions to Fulde–Ferrell–Larkin–Ovchinniko state. Starting at a high Zeeman field, above the Chandrasekhar–Clogston–Pauli limit (172, 173), $h_c = \Delta_{\mathrm{BCS}}/\sqrt{2}$ (a critical field for a direct first-order mean-field transition from an FL to a uniform BCS superconductor), inside the polarized FL and reducing h, one finds (in mean field) a continuous transition at $h_{c2} \approx \frac{3}{4}\Delta_{\mathrm{BCS}} > h_{\mathrm{c}}$ to an FFLO superconductor (1, 2, 131, 135) (stable for $h_{c1} < h < h_{c2}$), most strongly paired at a momentum with magnitude $p_0 \approx 1.2 h_{c2}/v_{\mathrm{F}} \approx 1.81 \Delta_{\mathrm{BCS}}/v_{\mathrm{F}}$. This is captured by a Ginzburg–Landau expansion [derived by integrating out the fermions (138)] for the ground-state energy density,

$$\mathcal{H} \approx \sum_{\mathbf{p}} \varepsilon_p |\Delta_{\mathbf{p}}|^2 + \sum_{\{\mathbf{p}_i\}} V_{\mathbf{p}_1,\mathbf{p}_2,\mathbf{p}_3,\mathbf{p}_4} \Delta^*_{\mathbf{p}_1} \Delta_{\mathbf{p}_2} \Delta^*_{\mathbf{p}_3} \Delta_{\mathbf{p}_4}, \quad 10.$$

which is valid for a weak finite-momentum pairing amplitude Δ_p near the continuous FL to FFLO phase transition at h_{c2}. It is notable that this expansion is analytic at small Δ_p, in contrast to a vanishing Zeeman field, that at zero temperature exhibits $|\Delta|^2 \ln \Delta$ nonanalyticity. The finite momentum instability is captured by the dispersion (131, 135, 138),

$$\begin{aligned}\varepsilon_p &\approx \frac{3n}{4\epsilon_F}\left[-1+\frac{1}{2}\ln\frac{v_F^2p^2-4h^2}{\Delta_{BCS}^2}+\frac{h}{v_Fp}\ln\frac{v_Fp+2h}{v_Fp-2h}\right],\\ &\approx J(p^2-p_0^2)^2+\varepsilon_{p_0}, \end{aligned} \quad 11.$$

whose minimum at a finite $p_0(h) \approx 1.2h/v_F$ (near h_{c2}) captures the polarized Fermi system's energetic tendency to pair at a finite momentum, forming an FFLO state at a fundamental reciprocal lattice vector with a magnitude p_0. The Zeeman energy h_{c2} at which $\varepsilon_{p_0}(h)$ vanishes determines the corresponding mean-field FL–FFLO phase transition point.

As in other problems of periodic ordering (e.g., crystallization), in the absence of an underlying lattice (as in trapped atomic gases) ε_p is rotationally invariant, and thus, the quadratic $|\Delta_{\mathbf{p}}|^2$ term only selects the fundamental *magnitude* of the reciprocal lattice, $|\mathbf{p}| = p_0$, with all degenerate orientations becoming unstable simultaneously at h_{c2}. This contrasts qualitatively with PDW ordering in solid state, where the underlying ionic crystal explicitly breaks rotational and translational symmetries, selecting a discrete set of $\mathbf{p}$ momenta, as discussed in Section 2. In the rotationally and translationally invariant trapped atomic gases, it is the quartic and higher-order nonlinearities in $\Delta_{\mathbf{p}}$ that select the structure of the FFLO state, characterized by the reciprocal lattice of $\mathbf{p}$'s and the corresponding amplitudes, $\Delta_{\mathbf{p}}$. Near h_{c2} it is the $(-\mathbf{p}, \mathbf{p})$ LO state (1) with $\Delta_{LO}(\mathbf{r}) = \Delta_{LO}\cos\mathbf{p}\cdot\mathbf{r}$ that is energetically preferred over the single plane-wave FF state, $\Delta_{FF}(\mathbf{r}) = \Delta_{FF}e^{i\mathbf{p}\cdot\mathbf{r}}$ (1, 2). However, no study has conclusively determined the structure of the FFLO state throughout the field-interaction (h - $1/k_Fa$) phase diagram, despite heroic efforts in the relativistic quantum chromodynamics context (180, 181).

Near h_{c2}, the unidirectional PDW (Cooper-pair stripe) order, characterized by a collinear set of $\mathbf{p}_n$'s, is well captured by focusing on long-wavelength fluctuations of these most unstable modes. The state is well described by a Ginzburg–Landau Hamiltonian density

$$\mathcal{H} = J\left[|\nabla^2\Delta|^2 - 2p_0^2|\nabla\Delta|^2\right] + r|\Delta|^2 + \frac{1}{2}\lambda_1|\Delta|^4 + \frac{1}{2}\lambda_2\mathbf{j}^2, \quad 12.$$

where deep in the BCS limit near h_{c2} the model parameters are given by

$$J \approx \frac{0.61n}{\epsilon_F p_0^4},\ p_0 \approx \frac{1.81\Delta_{BCS}}{\hbar v_F},\ r \approx \frac{3n}{4\epsilon_F}\ln\left[\frac{9h}{4h_{c2}}\right], \quad 13a.$$

$$h_{c2} \approx \frac{3}{4}\Delta_{BCS},\ \lambda_1 \approx \frac{3n}{4\epsilon_F\Delta_{BCS}^2},\ \lambda_2 \approx \frac{1.83nm^2}{\epsilon_F\Delta_{BCS}^2p_0^2}, \quad 13b.$$

and the inclusion of the current–current interaction, $\mathbf{j} = \frac{1}{m}\mathrm{Re}\,[-\Delta^*(\mathbf{r})i\nabla\Delta(\mathbf{r})]$, is necessary for a complete description of the transverse superfluid stiffness.

Well below h_{c2}, the PDW order parameter, $\Delta_{\mathbf{p}}$, is no longer small, invalidating the above Ginzburg–Landau expansion and requiring a complementary weak h Bogoliubov–de Gennes (BdG) treatment that is fully nonlinear in $\Delta(\mathbf{r})$. However, it is challenging to handle analytically for anything other than a single harmonic FF state, $\Delta_{FF}(\mathbf{r}) = \Delta_{FF}e^{i\mathbf{p}\cdot\mathbf{r}}$, as it requires a fully self-consistent BdG band-structure analysis, with energetics strongly dependent on the details of the FFLO state. A single-harmonic BdG calculation (131, 135) finds that a BCS singlet

superconductor is unstable to the FF state at $h_{c1} \approx 0.70\Delta_{BCS}$, thus suggesting that the PDW state is stable only over a very narrow range of h.

However, numerical BdG analyses (182–184) and a negative domain-wall energy in an otherwise fully paired singlet BCS superfluid in a Zeeman field (184, 185) argue that a more generic PDW state (that includes a larger set of collinear wavevectors) may be significantly more stable. Well below h_{c2} the FFLO state is thus more accurately described as a periodic array of solitons, well-paired $\pm\Delta_{BCS}$ stripes interrupted by "normal" gapless domain walls that accommodate the imposed fermion imbalance, driven by h. This state can be equivalently thought of as a periodically ordered microphase separation between the normal and paired states, that naturally replaces the macrophase separation (127, 186) ubiquitously found in the BCS-BEC detuning-imbalance phase diagram (131, 135, 136, 187) (see **Figure 11**). Upon increasing h above h_{c1}, the excess of the majority fermionic atoms (polarization) in an imbalanced system can be continuously accommodated by the subgap states localized on the self-consistently induced domain-walls between $+\Delta$ and $-\Delta$. Thus the imbalance and density of domain walls continuously grows above h_{c1}, eventually overlapping at h_{c2} and thereby interpolating between the two limiting forms of the LO state. This picture resembles the soliton mechanism for doping of polyacetylene (188), and it is explicitly realized in one-dimension through exact BdG (182) and Bethe ansatz (189, 190) solutions and via bosonization (191, 192) that exhibits the commensurate–incommensurate (CI) Pokrovsky–Talapov (PT) transition (193) from a fully paired s-wave superfluid to an LO state. Such phenomenology also emerges from the numerical BdG studies in two dimensions (183, 184). This response to a Zeeman field is quite analogous to the more familiar phenomenology of the type-II superconductor in an orbital magnetic field, with fully gapped BCS, partially paired FFLO, and fully depaired normal FL playing the role of the Meissner, Abrikosov vortex lattice and normal states, respectively.

5.2.3. Goldstone modes and topological excitations. Trapped atomic gases (in the absence of an optical lattice) exhibit underlying translational and rotational symmetries. Thus, as we discuss below, in addition to the off-diagonal-long-range order, the FFLO states break continuous spatial symmetries, and hence exhibit unusual Goldstone modes and novel topological defects. This contrasts qualitatively with the putative solid state PDW realizations (formulated in Section 2 and discussed in the rest of this review), where spatial symmetries are broken explicitly by the underlying crystal, and thus orientational Goldstone modes are absent.

Inspired by the 1D picture discussed above, a class of striped unidirectional FFLO, with Cooper pairs condensed at a colinear set of wavevectors $\mathbf{p}_n = n\mathbf{p}_0$, has received considerable attention. The FF plane wave and LO standing wave states are qualitatively accurate representatives, that have been extensively explored (9, 114). In particular, beyond mean-field theory, the time-reversal breaking FF state is characterized by an order parameter $\Delta_{FF}(\mathbf{r}) = \Delta_{p_0} e^{i\mathbf{p}_0\cdot\mathbf{r}+i\phi(\mathbf{r})}$, with a single Goldstone mode $\phi(\mathbf{r})$, that in addition to superfluid phase fluctuations also describes local fluctuations in the orientation of FF stripes. Because in a trapped atomic gas context, free of the underlying lattice, FF state spontaneously breaks rotational (but not translational) symmetry, the energetics of $\phi(\mathbf{r})$ is qualitatively "softer", with the Hamiltonian (derivable from the microscopics, above GL theory, or deduced based on symmetry),

$$\mathcal{H}_{FF} = \frac{1}{2}\chi^{-1}n^2 + \frac{1}{2}K(\nabla^2\phi)^2 + \frac{1}{2}\rho_s^{\parallel}(\partial_{\parallel}\phi)^2, \qquad 14.$$

where $\partial_{\parallel} \equiv \hat{\mathbf{p}}_0 \cdot \nabla$, $\rho_s^{||} = 8Jp^2|\Delta_{p_0}|^2$ is the superfluid stiffness along p_0, $K = 2J|\Delta_{p_0}|$, and n is the density operator (only well defined on a lattice), canonically conjugate to the phase field ϕ. The

spontaneous breaking of rotational symmetry requires a strict vanishing of FF's transverse superfluid stiffness, $\rho_s^{\perp} = 0$ (137, 138, 194).

The time-reversal preserving LO state spontaneously breaks both rotational and translational symmetries, with a $(-\mathbf{p}_0, \mathbf{p}_0)$ order parameter

$$\Delta_{LO}(\mathbf{r}) = 2\Delta_{p_0} e^{i\phi} \cos[\mathbf{p}_0 \cdot \mathbf{r} + \theta], \tag{15.}$$

that is a product of a superfluid parameter and a unidirectional density wave order parameter. These are characterized by two Goldstone modes, $\phi(\mathbf{r})$ and $\theta(\mathbf{r})$, corresponding to the superfluid phase and the smectic phonon $u(\mathbf{r}) = -\theta(\mathbf{r})/p_0$ of the striped state, respectively.

Similar to the FF state, the underlying rotational symmetry of the LO state strongly restricts the form of the Goldstone-mode Hamiltonian. Namely, its $\theta(\mathbf{r}) = -p_0 u(\mathbf{r})$ sector must be invariant under a rotation of $\mathbf{p}_0$, which defines the spontaneously chosen orientation of the PDW, and therefore must be described by a smectic form (195–197). However, because a rotation of the LO state leaves the SC phase, $\phi(\mathbf{r})$, unchanged, the superfluid phase $\phi(\mathbf{r})$ sector of the Hamiltonian is therefore expected to be of a conventional *xy*-model type. Consistent with these symmetry-based expectations, the LO Goldstone-mode Hamiltonian was indeed found (137, 138, 198, 199) to be given by

$$\begin{aligned}\mathcal{H}_{\mathrm{LO}} = &\frac{1}{2}\Pi^2 + \frac{1}{2}K(\nabla^2 u)^2 + \frac{1}{2}B(\partial_{\parallel} u)^2 \\ &+ \frac{1}{2}\chi^{-1} n^2 + \frac{1}{2}\rho_s^{\parallel}(\partial_{\parallel}\phi)^2 + \frac{1}{2}\rho_s^{\perp}(\nabla_{\perp}\phi)^2,\end{aligned} \tag{16.}$$

with Π being the momentum operator field, which is canonically conjugate to the phonon u. Thus, the LO state is a highly anisotropic superfluid (though less so than the FF state, where $\rho_s^{\perp} = 0$), with the ratio,

$$\frac{\rho_s^{\perp}}{\rho_s^{\parallel}} = \frac{3}{4}\left(\frac{\Delta_{\mathrm{p_0}}}{\Delta_{\mathrm{BCS}}}\right)^2 \approx \frac{1}{4}\ln\left(\frac{h_{c2}}{h}\right) \ll 1, \tag{17.}$$

that vanishes for $h \to h_{c2}^{-}$ (137, 138).

We note that in the presence of underlying rotational invariance, at nonzero temperature, the collinear FFLO states exhibit a 3D quasi-long-range translational order. Thus, the translational symmetry is restored, and somewhat oxymoronically, the FFLO order parameter $\Delta_{\mathbf{P}}$ vanishes inside a collinear FFLO phase. Consequently, the uniform Δ_{4e} is the fundamental nonzero order parameter at any nonzero temperature.

In addition to Goldstone modes, the low-energy phenomenology is also controlled by topological defects, that in conventional superfluids are limited to 2π vortices in the superfluid phase $\phi(\mathbf{r})$. In stark contrast, the additional LO phonon Goldstone mode $\theta(\mathbf{r})$ also admits 2π vortices, corresponding to an integer *a* dislocation in the striped LO order. Even more interesting, in addition to these integer vortex $(\pm 2\pi, 0)$ and dislocation $(0, \pm 2\pi)$ defects, the product nature of the LO order parameter (5.2.3) allows for half-integer vortex-dislocation composite defects $(\pm\pi, \pm\pi)$ (5, 7, 10, 137, 138), as is also discussed in Section 2.1. The sequential unbinding of this larger class of defects leads to a rich variety of LO descendent phases. Many interesting consequences such as 3D quasi-long-range order, importance of Goldstone-mode nonlinearities, charge-4*e* superconductivity, exotic topological phases, and transitions of the enriched nature of the FF and LO states have been extensively explored in References 114, 137, and 138.

Finally, we note that although the bosonic sector of the FFLO state discussed above is well understood, the problem is seriously complicated by the gapless fermions confined to the $\pm\Delta$ domain walls of the PDW. These will certainly lead to damping of the bosonic Goldstone modes. Coupling between the gapless fermions confined to strongly fluctuating FFLO phonons remain a challenging open problem, some aspects of which are discussed in Reference 138.

5.3. Nonuniform Pairing in Noncentrosymmetric and Weyl Superconductors

Nonuniform pairing states with an FFLO-like pairing mechanism have also been obtained in noncentrosymmetric systems (200, 201). In general these systems involve pairing on Fermi surfaces (FSs) whose centers do not sit at high symmetry points in the Brillouin zone, and thus the Cooper pairs forming from these FSs carry nonzero momentum.

One such scenario is for a metal with Rashba spin-orbit coupling in an in-plane Zeeman field H:

$$H = \frac{\mathbf{k}^2}{2m} - \mu + \lambda(\mathbf{k} \times \boldsymbol{\sigma}) \cdot \hat{\mathbf{z}} - \mu_B H \sigma_x. \qquad 18.$$

The SC instabilities of the concentric split FSs at $H = 0$ have been analyzed in Reference 202 (see also 203). With $H \neq 0$, in the limit $\mu_B H \ll \lambda k_F$, the two split FSs approximately retain their shapes and get relatively shifted by $\pm\mathbf{P}/2$, where $\mathbf{P} = \frac{2\mu_B H}{v_F}\hat{\mathbf{y}}$, shown in **Figure 13**. Naturally, the finite-momentum pairing order parameters couple as $\Delta_{\pm\mathbf{P}}\, c^\dagger(\mathbf{k} \pm \mathbf{P}/2)c^\dagger(-\mathbf{k} \pm \mathbf{P}/2)$, which separately gap out the two shifted split FSs. Compared with the FFLO scenario in which only a small part of the FS is gapped, the present state has a larger condensation energy and can potentially be realized at relatively small coupling.

Three pairing states have been theoretically investigated in References 200, 205, and 201: a uniform pairing order, an FF-like helical pairing order with only one ordering momentum (say $\Delta_{+\mathbf{P}}$), and an LO-like stripe pairing order with both $\Delta_{\pm\mathbf{P}}$. Note that unlike a canonical PDW state, where $\Delta_{\mathbf{P}}$ and $\Delta_{-\mathbf{P}}$ are related by inversion and time-reversal symmetry, here both symmetries are explicitly broken already in the normal state. In this case, symmetry arguments on the Ginzburg–Landau free energy imply the SC ground state generally has finite-momentum pairing (206, 207).

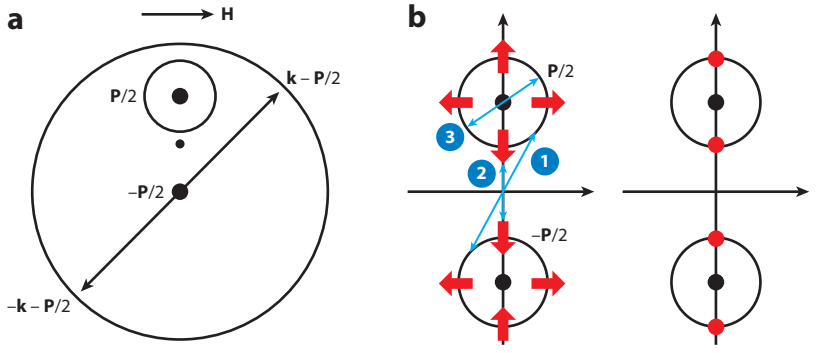

Figure 13

(*a*) The split FSs described by Equation 18. (*b*) (*Left*) Spin texture on the Weyl FSs, and various Cooper pairs. Arrows ❶ and ❷ show Cooper pairs in a uniform SC state, but for arrow ❷ the fermions have the same spin, and a singlet pairing gap vanishes here. Arrow ❸ shows the Cooper pairs in a PDW state with intra-FS pairing. (*Right*) The point nodes in the spin-singlet pairing state. Abbreviations: FS, Fermi surface; SC, superconducting. Panel *a* adapted from Reference 200, and panel *b* from Reference 204.

In microscopic studies, it was indeed obtained that the finite-momentum pairing orders including helical order and stripe order occupy sizable regions in the pairing phase diagram as a function of temperature and the in-plane Zeeman field (200, 201, 208). Properties of these nonuniform pairing states in noncentrosymmetric materials have been reviewed in Reference 209.

Signatures of such a stripe PDW-like state were indeed observed in proximitized HgTe quantum wells (210). When gated to the electron-doped regime, the HgTe quantum well exhibits split FSs with Rashba spin-orbit coupling. The quantum well is coupled to a conventional superconductor on one side and subject to an in-plane magnetic field **B**. As **B** varies, the oscillation of the Josephson current across the quantum well has been observed, which is evidence for finite-momentum pairing order induced in HgTe. The in-plane Zeeman field can be either an external field or realized intrinsically. In Reference 211, PDW pairing has been proposed for $SrTiO_3$–$LaAlO_3$ oxide interfaces, which exhibit coexistence between ferromagnetism and SC orders. It was shown that the effective interaction between the local moments drive the interface into a ferromagnetic phase. Together with the Rashba spin-orbit coupling, the system was proposed to realize a PDW-like state via the aforementioned mechanism. Another context of this mechanism for nonuniform pairing is the surface superconductivity on topological insulators (TIs). Much of the attention toward TI-surface superconductivity has been focused on its realization of topological superconductivity, i.e., the well-known Fu–Kane superconductivity (212). However, with a nonzero chemical potential, the surfaces also host $\pm\mathbf{P}/2$-shifted FSs with a spin texture (213). However, unlike the FS in **Figure 13**, the two FSs are located at opposite spatial surfaces. Furthermore, inversion symmetry is not necessarily broken in the 3D system, thus the two FSs can have the same size. Remarkably, there is recent experimental evidence observing finite-**P** pairing on TI surfaces with an in-plane Zeeman field (214).

An interesting extension of this mechanism for the nonuniform pairing state is to 3D systems with FSs not centered around any high symmetry points $\pm\mathbf{P}/2$ (204, 215–217). The simplest way of obtaining these FSs is from doping a Weyl semimetal, which does not require any symmetry to stabilize. A simple two-band lattice model given by Reference 204 describing this situation is

$$H_0 = t(\sigma^x \sin k_x + \sigma^y \sin k_y) + t_z[\cos k_z - \cos(P/2)]\sigma^z + m(2 - \cos k_x - \cos k_y)\sigma^z - \mu. \qquad 19.$$

For small chemical potential μ, each spherical FS encloses a Weyl point at $\pm\mathbf{P}/2$ and is spin textured, analogous to the 2D case with Rashba spin-orbit coupling (see **Figure 13*a*** for a $k_y = 0$ slice).

Both intra-FS and inter-FS pairing can potentially occur, giving rise to a PDW-like state with ordering momenta $\pm\mathbf{P}$ and a uniform SC state, respectively. The energetic interplay between PDW and a uniform superconductor depends on several factors. First, unlike the previous case in which the FSs remain symmetric about their shifted centers for small H, here in general there is no symmetry relating $\epsilon(\mathbf{k} + \mathbf{P}/2)$ and $\epsilon(-\mathbf{k} + \mathbf{P}/2)$ unless μ is very small. Either way, the susceptibility toward a PDW state is reduced, whereas typically inversion symmetry (for the present case with two Weyl nodes) or time-reversal symmetry (e.g., for cases with four Weyl nodes) guarantees a weak-coupling instability toward a uniform superconductor. By contrast, there is a robust topological reason that the uniform SC order parameter has point nodes, which tends to suppress the uniform superconductor. This was first observed in Reference 204 and formulated in generic cases in Reference 216. Weyl points are monopoles of the Berry curvature $\vec{\mathcal{B}}(\mathbf{k}) = \mathbf{i}\langle\nabla_{\mathbf{k}}\mathbf{u}(\mathbf{k})| \times |\nabla_{\mathbf{k}}\mathbf{u}(\mathbf{k})\rangle$ in $\mathbf{k}$ space. Weyl points at $\pm\mathbf{P}/2$ carry monopole charges ± 1, and this monopole charge is equal to the Berry flux through its enclosing FS. In the Nambu space of the pairing Hamiltonian, the Berry fluxes through the electron-like FS and hole-like shadow FS are subject to pairing, and the monopole charges add up. It was shown that (216, 217) the total monopole charge inside the original FS is 2 for uniform (inter-FS) SC, and it is 0 for (intra-FS) PDW. This means that the uniform

SC state has to host at least two point nodes on each FS, independent of any microscopic details. The PDW state can be fully gapped, likely leading to a higher condensation energy.

The detailed interplay between these two opposite effects has been examined in Reference 215 with short-range attractive interactions in PDW and SC channels, and the authors found that a PDW state is favored for a noncentrosymmetric Weyl metal. However, in more realistic systems a more careful examination on the band structure and the interaction is needed to pin down the SC ground state.

6. BROADER RELEVANCE FOR THE CUPRATE SUPERCONDUCTORS

In the preceding sections, we presented evidence of the existence of PDW SC order in diverse systems ranging from cuprate high-temperature superconductors to heavy fermionic materials, to organics, to topological materials, as well as in cold atomic systems. Unlike its FFLO predecessors, the PDW discussed in the context of the cuprate family does not require an external magnetic field for its existence.

As reviewed in earlier sections, the PDW is a new state of matter with unique properties not encountered in other superconductors. It is an SC state with more than one complex order parameter. Its more complicated order parameter manifold allows this state to accommodate various charge orders, together with SC states, some even with an exotic flux quantization. This richness leads, in a natural way, to an explanation of several intriguing experimental effects, such as dynamical layer decoupling and a rich structure of SC vortices. These features also imply a complex phase diagram with a variety of broken symmetry phases.

Given the evidence that PDW order appears in some places in the cuprate phase diagram, it remains to discuss the implication of this observation in the broader context of cuprate physics (and beyond). Up to now the evidence comes primarily from two groups of experiments on two groups of materials. First, as reviewed in Section 3.1, there is the layer decoupling observed in 1/8-doped LBCO, which led to the PDW concept. This suggestion has been leant further credibility by the observation of a variety of other related phenomena, such as the detection of an anomalously large second harmonic in the Josephson relation in LBCO-Nb junctions and the appearance of the familiar signatures of layer decoupling in other 214 materials when stripe order is enhanced, including LSCO in a magnetic field. Second, a CDW with wave-vector equal to half of what is commonly observed was seen in the vicinity of the vortex core in underdoped Bi-2212 (14). As such a CDW subharmonic is expected as a consequence of coexisting uniform and PDW order; its observation provides strong evidence of the existence of PDW in the vortex halo, as discussed in Section 3.2.

It is worth mentioning that none of these pieces of evidence is entirely immune to the possibility of alternative explanations; indeed, in all cases there are additional experimental observations that, while not actually contradictory with the PDW interpretation, are also not entirely natural. Most important, to date no diffraction experiments have detected the expected CDW subharmonic associated with the coexistence of PDW and uniform SC correlations, either in LBCO or in the magnetic field and temperature regimes that have been so far explored in YBCO and BSCCO. Conversely, in the range of T in which layer decoupling gives strong evidence of dominantly PDW correlations in 1/8-doped LBCO, ARPES data have been interpreted (218, 219; see **Figure 14**) as showing a nodal-*d*-wave-like one-electron spectrum, rather than the nodal-arc spectrum expected for a pure PDW (similar two-gap ARPES spectra have been seen in BSCCO) (219, 220; see **Figure 15**). In all cases, there are multiple possible ways one can imagine reconciling these observations with the PDW interpretation. However, ultimately we rely on further experiments (some of which are discussed below) to resolve these issues.

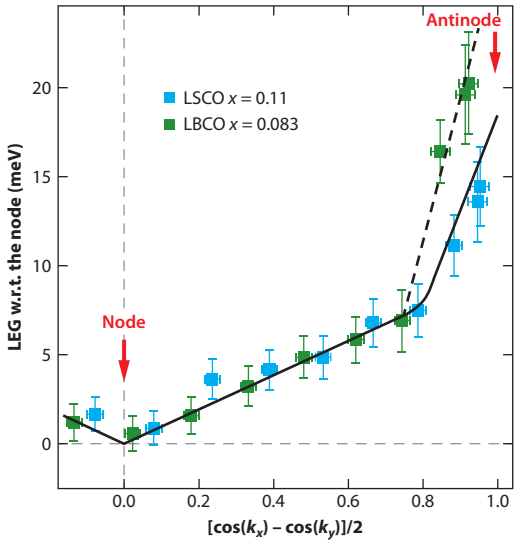

Figure 14

Momentum-dependent gap of LBCO and LSCO from ARPES experiments by Vishik et al. (219). Abbreviations: ARPES, angle-resolved photoemission spectroscopy; LBCO, $La_{2-x}Ba_xCuO_4$; LEG, leading edge gap; LEM, leading edge midpoint; LSCO, $La_{2-x}Sr_xCuO_4$. Figure adapted from Reference 219.

Putting these concerns aside, a key question is whether these PDW sightings are relevant only in the relatively narrow context of cuprates with certain structural peculiarities (such as LBCO) or in the vicinity of isolated vortex cores, or whether they have broader implications to the physics of underdoped cuprates. In particular, there is the question of whether PDW correlations are in

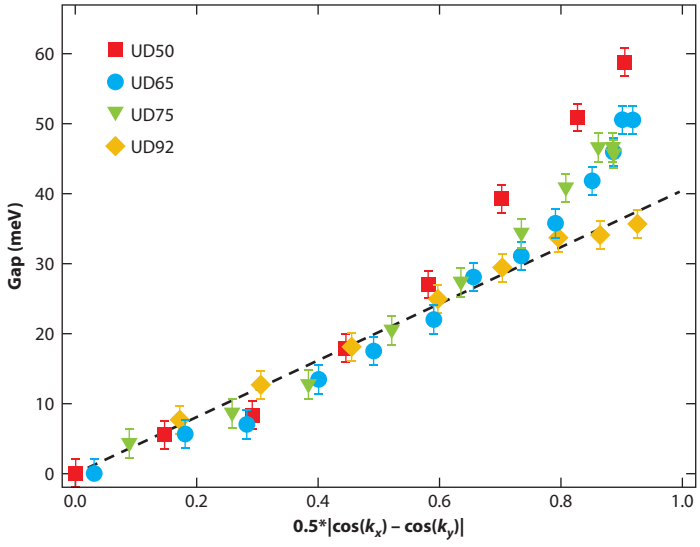

Figure 15

Momentum-dependent gap in $Bi_2Sr_2CaCu_2O_{8+\delta}$ from ARPES experiments by Vishik et al. (219). Abbreviation: ARPES, angle-resolved photoemission spectroscopy. Figure adapted from Reference 219.

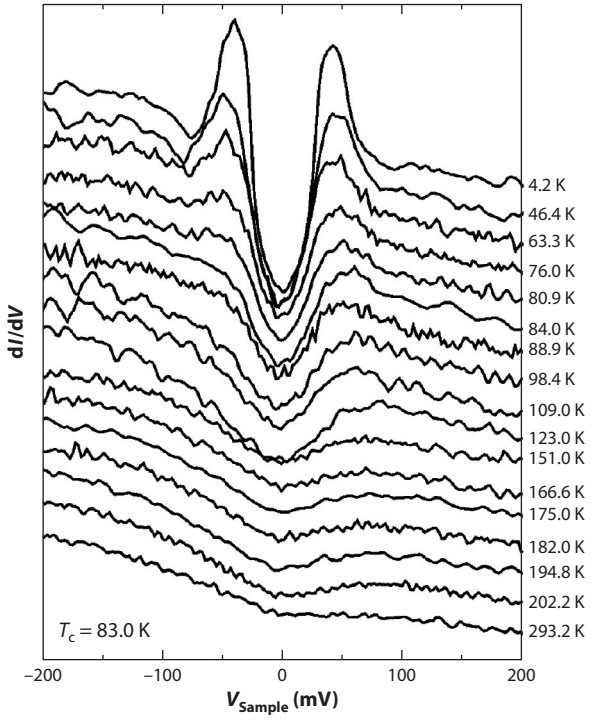

Figure 16

Pseudogap in $Bi_2Sr_2CaCu_2O_{8+\delta}$ from scanning tunneling microscopy experiments by Renner et al. Figure adapted from Reference 221.

any way responsible for the so-called pseudogap regime observed in underdoped cuprates. For the purpose of this review, we focus the discussion of this question on the range of hole doping from $p \sim 0.08$ to 0.15 in which there is an identifiable temperature scale, T^*, below which various measurable properties show a depletion of the density of states at low energies. This thus pertains to an intermediate doping range between the very low-doping region, where physics is dominated by significant local antiferromagnetic order, and the high-doping region, where a full FS enclosing $1 + p$ holes forms. Note that T^* is at largest 300 K–400 K, which is still low compared with microscopic scales such as the exchange scale J. A phenomenon closely associated with this T^* scale is the appearance of a deep depression in the single-particle spectral weight (i.e., the eponymous pseudogap) in the antinodal portion of the Fermi surface up to T^*, which in turn can be much higher than T_c. This pseudogap has been seen not only in ARPES data but also by STM, as shown in **Figure 16**; importantly, because STM accesses both the unoccupied and occupied states, it reveals an approximate particle–hole symmetry of this gap. This suggests that the gap is associated with some form of SC pairing. However, certain features of the gap as inferred from ARPES evolve differently as a function of doping and temperature in the near nodal region, where the gap is small, and in the antinodal region, where it is large—this is the so-called nodal–antinodal dichotomy. This can be seen to some extent in the data from Bi2212 shown in **Figure 15**, and more dramatically in the case of LBCO (**Figure 14**) and Bi-2201, where detailed ARPES data are available (27). This apparent dichotomy has led many researchers to conclude that the pseudogap has a distinct (nonsuperconducting) origin.

In addition to the energy gap, another striking feature of the underdoped cuprate phase diagram is the existence of "intertwined" order parameters corresponding to multiple distinct broken symmetry states that occur with similar energy and temperature scales and which in some ways compete and in some ways cooperate strongly with each other. In addition to the insulating Néel order and uniform *d*-wave SC order, this list includes a variety of other metallic or SC SDW, CDW, and nematic orders. To this list we now add PDW order. It is unreasonable that these materials should be accidentally fine-tuned close to an extraordinarily complex multicritical point at which all these orders are degenerate with each other, so it is reasonable to search for a description in which the observed orders derive from a smaller set of primary order parameters.

The underlying idea is that, under certain circumstances, some class of soft fluctuations can partially melt a parent broken symmetry state in such a way that some but not all the underlying symmetries are restored, leaving behind a partially ordered state with some form of vestigial order (25). Formally, as discussed in Section 2, this corresponds to forming composite order parameters that are bilinear (or higher order) in the primary order parameter fields. In the present context, starting from an assumed primary PDW order parameter, one can readily construct composite orders corresponding to both CDW order and nematic orders, making it possible to view these as remaining vestigial orders when a fully ordered PDW is partially melted by strong phase fluctuations.

There are several phenomenologically appealing aspects of this perspective. With regards to nematic order, though there is suggestive evidence that it arises at temperature scales comparable with the pseudogap T^*, it is very difficult to see how a primary nematic order could be responsible for the pseudogap, but viewed as a composite order, it can be understood as an avatar of a more basic set of correlations. Similarly, the observed CDW order is mostly weak in the sense that it causes unusually small magnitude lattice distortions, which is why it was overlooked for so many years. (LBCO may be an exception.) The CDW does not open gaps or fold the FS observed in ARPES in ways that are familiar from other classes of CDW materials (27). Still, CDW order appears to be thermodynamically robust in both the sense that significant CDW correlations persist over a wide range of T and p and that it competes on a more or less equal footing with the uniform *d*-wave SC state, for instance in that there is a clear suppression of the SC T_c in the range of dopings where the CDW correlations are strongest, whereas high T_c can be restored with the application of modest pressure, presumably because this suppresses the CDW tendency. Again, viewing the CDW as a composite order gives a rationale for viewing it as being simultaneously weak and strong in different aspects.

At a more local level, there has long been strong intuitive appeal to viewing the pseudogap as a form of local pairing without any significant SC phase coherence. The fact that the pseudogap shares so many obvious similarities with the *d*-wave SC gap is, of course, the strongest piece of evidence in favor of this interpretation. For instance, at low temperatures, the gap magnitude along the FS seen in ARPES in Bi-2212 for doping roughly in the range of $0.12 < p < 0.19$ has the simplest *d*-wave form, $\Delta_0\{[\cos(k_x) - \cos(k_y)]/2\}$. This gap is well understood as being due to the *d*-wave SC state. However, there is a distinct difference in the thermal evolution of the near nodal and antinodal gaps; this is an aspect of the previously mentioned nodal–antinodal dichotomy. In particular, in the antinodal regime of the Brillouin zone, the gap magnitude is only very weakly T dependent and it evolves smoothly into the pseudogap that persists to well above T_c. Furthermore, shown in **Figure 15** as a function of decreasing p, the energy gap below T_c at the antinode starts to grow strongly but continuously; i.e., the gap structure increasingly looks like the sum of a near-nodal SC gap (whose magnitude is in fact largely independent of p down to $p \approx 0.07$) plus another gap that is large at the antinode and small or vanishing in an arc region near the nodal point. In the context of the present work, it is tempting to associate this evolution with an increasingly significant

admixture of a PDW component in the gap structure. Also, at least in Bi-2201 for which detailed ARPES spectra are available, the top of the gap does not line up with the location of the Fermi momentum, as one would expect for a uniform superconductor, but it is consistent with a momentum-carrying condensate, such as the PDW (7, 27). Although it may be possible to account for the differences in the thermal evolution of the gap in the nodal and antinodal regimes as a purely kinematic effect of phase fluctuations in a simple *d*-wave superconductor (222, 223), the nodal–antinodal dichotomy has been taken as evidence against fluctuating *d*-wave as the origin of the pseudogap at the antinode (219, 224). The PDW seems like a natural candidate that is next in line.

To summarize, there remains the larger question of the broader significance of the PDW in the phase diagram of the cuprates and, particularly, of its role in the pseudogap regime. We find it useful to focus on two extremal perspectives that lie at the opposite ends of a spectrum of possibilities. For ease of discussion, we label the first view as competing order and the second view as mother state.

In the competing order perspective, the PDW is a close competitor of uniform *d*-wave superconductivity and of the observed CDW orders, which are to be regarded as independent (although strongly coupled) order parameters. Their interplay may change from one family of cuprates to another (or in a particular family as a function of doping) depending on other factors, e.g., the crystal structure, whether SDW order plays a role or not, etc. This is especially clear in the case of LBCO, where the critical temperatures are comparable, which naturally leads to the notion that they may have a common microscopic origin (and, in this sense, are intertwined). Nevertheless, this does not necessarily imply that they should not be regarded as completely separate orders. This is because there are terms in the Landau theory of the type presented in earlier sections, e.g., trilinear couplings of the form $\rho_{2\mathbf{P}}\Delta^*_{\mathbf{P}}\Delta_{-\mathbf{P}}$. Physically, these terms can be interpreted as saying that there should be a nonvanishing value of the CDW order $\rho_{2\mathbf{P}}$ as soon as the PDW order parameter is present, $|\Delta_{\pm\mathbf{P}}| \neq 0$, i.e., $\rho_{\mathbf{P}} \propto \Delta^*_{-\mathbf{P}}\Delta_{\mathbf{P}}$, and the CDW order is a composite order. However, this coupling can also be interpreted as saying that as $\rho_{2\mathbf{P}}$ becomes sufficiently strong, the quadratic term of the PDW order can aquire a negative coefficient that, when large enough, can induce a PDW order parameter $\Delta_{\pm\mathbf{P}}$.

A convenient mathematical language to describe competing order is the nonlinear σ model. This has been employed to describe the appearance of static PDW in the vicinity of the vortex core, where *d*-wave order smoothly rotates to a PDW order (12). Another situation for its application may be the onset of layer decoupling driven by a magnetic field in LSCO (48). In that case, one may envision a rotation to a PDW from a *d*-wave under the influence of magnetic-field-driven spin order.

A second perspective is to regard the PDW as the primary order (the mother state), and to regard other orders (e.g., CDW) as composite (or descendant) orders. If the low-temperature phase is indeed a PDW, then the other orders may appear through a partial melting cascade of phase transitions. In these regimes, the CDW (and nematic) orders are vestigial orders of the PDW, and the PDW itself can be regarded as a fluctuating order.

As a fluctuating order, the PDW is locally defined on some length scale without ever being the ground state. The correlation length should be long enough to form the antinodal gap and to induce the composite orders, but short enough that the properties usually associated with superfluidity are not apparent. Taken to its logical conclusion, this point of view states that PDW fluctuations are pervasive over a large part of the doping, temperature, and magnetic field range of the phase diagram and are the root cause of the pseudogap phenomenology. This view has been strongly advocated by one of us (7), whereas a more guarded proposal has been made that fluctuating PDW may be responsible for the pseudogap structure at the antinode and the Fermi arc near the node (6). The appeal of this picture is that it reduces the explanation of the panoply of

observed orders to the existence of local PDW orders. The rapid winding of the *d*-wave vortex has been suggested to pin the PDW near the vortex core, rendering it static and generating the short range CDW with wavevector **P** observed in STM experiments (225). Just as in the competing order scenario, the PDW provides a mechanism for lowering the vortex core energies and, hence, making H_{c2} parametrically smaller (12). What happens for fields greater than H_{c2} is probably the most intriguing open question. One has to face the question of how to describe a pairing state that has been destroyed by quantum phase fluctuations, which remains unsolved (226). The quantum disordering of a PDW that already breaks translational symmetry and is gapless even in the absence of a magnetic field is still more clearly *terra incognita*. Experimentally, CDW with longer-range order appears with increasing magnetic field, and a metallic state with a small Fermi pocket emerges. Whether this state can be the result of a fluctuating PDW remains to be seen (6, 7, 11, 28, 227–230). It is worth noting that the competing order scenario faces the same issue: In the nonlinear sigma-model description (12), an ordered PDW appears when the vortex halos overlap and one needs to address the question of how this order is destroyed.

Another important question for the mother state scenario is whether a coherence length large enough to create an energy gap will necessarily produce large observable consequences of SC fluctuations. Experimentally diamagnetic fluctuations have been observed at up to two or three times T_c and also above H_{c2} at low temperatures (231, 232). However, there is little in the way of transport signatures. Can these observations be reconciled? The ultimate question is whether these ideas and the contrast between the two extreme perspectives can be either directly supported or falsified. In this sense the recent proposal of a method to directly measure PDW fluctuations in a tunnel junction using Bi-2201 as one electrode and then taking advantage of the known momentum that is present in this material offers some hope for the future (233).

Finally, it is important to determine the extent to which the 1**P** CDW observed so far by STM in Bi-2212 can be detected with other probes and in other cuprate families. We note that several groups have searched for, but so far failed to find, evidence of a subharmonic CDW **P** peak in X-ray diffraction in the SC state of high T_c cuprates in which CDW order is known to be present. So far unpublished X-ray searches for a **P** peak have been carried out in 15.5% doped $La_{2-x}Ba_xCuO_4$ (P. Abbamonte, private communication) and in $YBa_2Cu_3O_{6+x}$ at relatively low temperatures in magnetic fields of ~6 T (234). Data from other experiments in $Bi_2(Sr, La)_2CuO_{6+\delta}$ at zero magnetic field (235, 236) also do not show evidence for this peak. It would be interesting to extend the X-ray searches to regimes in which the layer decoupling effect, an indicator of PDW order, has already been seen, such as in underdoped $La_{2-x}Sr_xCuO_4$ (48) in a magnetic field and $La_{2-x}Ba_xCuO_4$ (237), or in SC $Bi_2Sr_2CaCu_2O_{8+\delta}$ in the regime in which STM experiments see the peak at wavevector **P** peak in vortex halos (14).

DISCLOSURE STATEMENT

The authors are not aware of any affiliations, memberships, funding, or financial holdings that might be perceived as affecting the objectivity of this review.

ACKNOWLEDGMENTS

J.C.S.D. acknowledges support from Science Foundation Ireland under Award SFI 17/RP/5445 and from the European Research Council (ERC) under Award DLV-788932. J.C.S.D and S.D.E acknowledge support, and the funding to carry out STM/SJTM studies of cuprate PDWs, from the Gordon and Betty Moore Foundation EPiQS Initiative through Grant GBMF4544. S.D.E.

acknowledges support from the Karel Urbanek Postdoctoral Fellowship at Stanford University. S.A.K. was supported in part by National Science Foundation (NSF) grant DMR-1608055. E.F. was supported in part by NSF grant DMR-1725401. This work was funded by the Office of Basic Energy Sciences, Materials Sciences and Engineering Division, US Department of Energy (DOE) under contracts DE-SC0012368 (D.J.V.H., E.F.). D.J.V.H. was supported in part by NSF grant DMR-1710437. P.A.L. acknowledges support by DOE grant DE-FG02-03ER46076. Y.W. was supported by the Gordon and Betty Moore Foundation EPiQS Initiative through the grant GBMF 4305. L.R. was supported by the Simons Investigator Award from The James Simons Foundation. J.M.T. was supported at Brookhaven by DOE Contract No. DE-SC0012704. This research was supported in part by the NSF under Grant No. NSF PHY-1748958 at the Kavli Institute for Theoretical Physics of the University of California, Santa Barbara, and we thank KITP for its hospitality.

LITERATURE CITED

1. Larkin AI, Ovchinnikov YN. 1965. *Sov. Phys. J. Exp. Theor. Phys.* 20:762
2. Fulde P, Ferrell RA. 1964. *Phys. Rev.* 135:A550–63
3. Himeda A, Kato T, Ogata M. 2002. *Phys. Rev. Lett.* 88:117001
4. Berg E, Fradkin E, Kim EA, Kivelson SA, Oganesyan V, et al. 2007. *Phys. Rev. Lett.* 99:127003
5. Agterberg DF, Tsunetsugu H. 2008. *Nat. Phys.* 4:639–42
6. Berg E, Fradkin E, Kivelson SA, Tranquada JM. 2009. *New J. Phys.* 11:115004
7. Lee PA. 2014. *Phys. Rev. X* 4:031017
8. Casalbuoni R, Nardulli G. 2004. *Rev. Mod. Phys.* 76:263–320
9. Kinnunen JJ, Baarsma JE, Martikainen JP, Törma P. 2018. *Rep. Prog. Phys.* 81:046401
10. Berg E, Fradkin E, Kivelson SA. 2009. *Nat. Phys.* 5:830–33
11. Agterberg DF, Garaud J. 2015. *Phys. Rev. B* 91:104512
12. Wang Y, Edkins SD, Hamidian MH, Davis JCS, Fradkin E, Kivelson SA. 2018. *Phys. Rev. B* 97:174510
13. Dai Z, Zhang YH, Senthil T, Lee PA. 2018. *Phys. Rev. B* 97:174511
14. Edkins SD, Kostin A, Fujita K, Mackenzie AP, Eisaki H, et al. 2019. *Science* 364:976–80
15. Fradkin E, Kivelson SA, Tranquada JM. 2015. *Rev. Mod. Phys.* 87:457–82
16. Agterberg DF, Sigrist M, Tsunetsugu H. 2009. *Phys. Rev. Lett.* 102:207004
17. Radzihovsky L, Vishwanath A. 2009. *Phys. Rev. Lett.* 103:010404
18. Radzihovsky L. 2011. *Phys. Rev. A* 84:023677
19. Barci DG, Fradkin E. 2011. *Phys. Rev. B* 83:100509
20. Mross DF, Senthil T. 2015. *Phys. Rev. X* 5:031008
21. Berezinskii V. 1972. *Sov. Phys. J. Exp. Theor. Phys.* 34:610–16
22. Kosterlitz J, Thouless D. 1973. *J. Phys. C* 6:1181–204
23. Jose J, Kadanoff L, Kirkpatrick S, Nelson D. 1977. *Phys. Rev. B* 16:1217–41
24. Chen HD, Vafek O, Yazdani A, Zhang SC. 2004. *Phys. Rev. Lett.* 93:187002
25. Nie L, Tarjus G, Kivelson SA. 2014. *PNAS* 111:7980–85
26. Chan C. 2016. *Phys. Rev. B* 93:184514
27. He R, Hashimoto M, Karapetyan H, Koralek J, Hinton J, et al. 2011. *Science* 331:1579–83
28. Baruch S, Orgad D. 2008. *Phys. Rev. B* 77:174502
29. Harrison N, Sebastian S. 2011. *Phys. Rev. Lett.* 106:226402
30. Wang Y, Agterberg DF, Chubukov A. 2015. *Phys. Rev. Lett.* 114:197001
31. Tu WL, Lee TK. 2019. *Sci. Rep.* 9:1719
32. Moodenbaugh AR, Xu Y, Suenaga M, Folkerts TJ, Shelton RN. 1988. *Phys. Rev. B* 38:4596–600
33. Fujita M, Goka H, Yamada K, Tranquada JM, Regnault LP. 2004. *Phys. Rev. B* 70:104517
34. Hücker M, v. Zimmermann M, Gu GD, Xu ZJ, Wen JS, et al. 2011. *Phys. Rev. B* 83:104506
35. Axe JD, Moudden AH, Hohlwein D, Cox DE, Mohanty KM, et al. 1989. *Phys. Rev. Lett.* 62:2751–54

36. Axe JD, Crawford MK. 1994. *J. Low Temp. Phys.* 95:271–84
37. Li Q, Hücker M, Gu GD, Tsvelik AM, Tranquada JM. 2007. *Phys. Rev. Lett.* 99:067001
38. Tranquada JM, Gu GD, Hücker M, Jie Q, Kang HJ, et al. 2008. *Phys. Rev. B* 78:174529
39. Li Q, Hücker M, Gu GD, Tsvelik AM, Tranquada JM. 2007. *Phys. Rev. Lett.* 99:067001
40. Tranquada JM, Sternlieb BJ, Axe JD, Nakamura Y, Uchida S. 1995. *Nature* 375:561–63
41. Tajima S, Noda T, Eisaki H, Uchida S. 2001. *Phys. Rev. Lett.* 86:500–3
42. Basov DN, Timusk T. 2005. *Rev. Mod. Phys.* 77:721–79
43. Croft TP, Lester C, Senn MS, Bombardi A, Hayden SM. 2014. *Phys. Rev. B* 89:224513
44. Thampy V, Dean MPM, Christensen NB, Steinke L, Islam Z, et al. 2014. *Phys. Rev. B* 90:100510
45. Suzuki T, Goto T, Chiba K, Shinoda T, Fukase T, et al. 1998. *Phys. Rev. B* 57:R3229–32
46. Kimura H, Matsushita H, Hirota K, Endoh Y, Yamada K, et al. 2000. *Phys. Rev. B* 61:14366–69
47. Lake B, Rønnow HM, Christensen NB, Aeppli G, Lefmann K, et al. 2002. *Nature* 415:299–301
48. Schafgans AA, LaForge AD, Dordevic SV, Qazilbash MM, Padilla WJ, et al. 2010. *Phys. Rev. Lett.* 104:157002
49. Wen J, Jie Q, Li Q, Hücker M, v. Zimmermann M, et al. 2012. *Phys. Rev. B* 85:134513
50. Stegen Z, Han SJ, Wu J, Pramanik AK, Hücker M, et al. 2013. *Phys. Rev. B* 87:064509
51. Zhong R, Schneeloch JA, Chi H, Li Q, Gu G, Tranquada JM. 2018. *Phys. Rev. B* 97:134520
52. He RH, Tanaka K, Mo SK, Sasagawa T, Fujita M, et al. 2009. *Nat. Phys.* 5:119–23
53. Valla T, Federov AV, Lee J, Davis JC, Gu GD. 2006. *Science* 314:1914–16
54. Razzoli E, Drachuck G, Keren A, Radovic M, Plumb NC, et al. 2013. *Phys. Rev. Lett.* 110:047004
55. Loder F, Graser S, Schmid M, Kampf AP, Kopp T. 2011. *Phys. Rev. Lett.* 107:187001
56. Homes CC, Hücker M, Li Q, Xu ZJ, Wen JS, et al. 2012. *Phys. Rev. B* 85:134510
57. Li Y, Terzic J, Baity PG, Popović D, Gu GD, et al. 2018. *Sci. Adv.* 5:eaav7686
58. Rajasekaran S, Okamoto J, Mathey L, Fechner M, Thampy V, et al. 2018. *Science* 359:575–79
59. Yuli O, Asulin I, Millo O, Koren G. 2007. *Phys. Rev. B* 75:184521
60. Yang KY, Chen WQ, Rice TM, Sigrist M, Zhang FC. 2009. *New J. Phys.* 11:055053
61. Yuli O, Asulin I, Koren G, Millo O. 2010. *Phys. Rev. B* 81:024516
62. Yang K. 2013. *J. Supercond. Nov. Magn.* 26:2741–42
63. Shi Z, Baity PG, Terzic J, Sasagawa T, Popović D. 2019. arXiv:1907.11708
64. Buzdin A, Koshelev AE. 2003. *Phys. Rev. B* 67:220504
65. Moshe M, Mints RG. 2007. *Phys. Rev. B* 76:054518
66. Stoutimore MJA, Rossolenko AN, Bolginov VV, Oboznov VA, Rusanov AY, et al. 2018. *Phys. Rev. Lett.* 121:177702
67. Schneider CW, Hammerl G, Logvenov G, Kopp T, Kirtley JR, et al. 2004. *Europhys. Lett.* 68:86
68. Hamilton DR, Gu GD, Fradkin E, Van Harlingen DJ. 2018. *Phys. Rev. B*. In press. arXiv:1811.02048
69. Fujita K, Hamidian M, Firmo I, Mukhopadhyay S, Kim CK, et al. 2015. In *Strongly Correlated Systems, Springer Series in Solid-State Sciences*, Vol. 180, ed. A Avella, F Mancini, pp. 73–109. Berlin, Heidelberg: Springer
70. Hoffman JE, Hudson EW, Lang KM, Madhavan V, Eisaki H, et al. 2002. *Science* 295:466–69
71. Matsuba K, Yoshizawa S, Mochizuki Y, Mochiku T, Hirata K, Nishida N. 2007. *J. Phys. Soc. Jpn.* 76:063704
72. Yoshizawa S, Koseki T, Matsuba K, Mochiku T, Hirata K, Nishida N. 2013. *J. Phys. Soc. Jpn.* 82:083706
73. Machida T, Kohsaka Y, Matsuoka K, Iwaya K, Hanaguri T, Tamegai T. 2016. *Nat. Commun.* 7:1–6
74. Pan SH, Hudson EW, Davis JC. 1998. *Appl. Phys. Lett.* 73:2992–94
75. Naaman O, Teizer W, Dynes RC. 2001. *Phys. Rev. Lett.* 87:097004
76. Rodrigo JG, Suderow H, Vieira S. 2004. *Eur. Phys. J. B* 40:483–88
77. Proslier Th, Kohen A, Noat Y, Cren T, Roditchev D, Sacks W. 2006. *Europhys. Lett.* 73:962–68
78. Randeria MT, Feldman BE, Drozdov IK, Yazdani A. 2016. *Phys. Rev. B* 93:161115
79. Hamidian M, Edkins S, Joo SH, Kostin A, Eisaki H, et al. 2016. *Nature* 532:343–47
80. Hanaguri T, Lupien C, Kohsaka Y, Lee DH, Azuma M, et al. 2004. *Nature* 430:1001–5
81. McElroy K, Lee DH, Hoffman JE, Lang KM, Lee J, et al. 2005. *Phys. Rev. Lett.* 94:197005
82. Kohsaka Y, Taylor C, Fujita K, Schmidt A, Lupien C, et al. 2007. *Science* 315:1380–85

83. Mesaros A, Fujita K, Edkins SD, Hamidian MH, Eisaki H, et al. 2016. *PNAS* 113:12661–66
84. Zhang Y, Mesaros A, Fujita K, Edkins SD, Hamidian MH, et al. 2019. *Nature* 570:484–90
85. Hamidian MH, Edkins SD, Kim CK, Davis JC, Mackenzie AP, et al. 2015. *Nat. Phys.* 12:150–56
86. Fujita K, Hamidian MH, Edkins SD, Kim CK, Kohsaka Y, et al. 2014. *PNAS* 111:E3026–32
87. Agosta C. 2018. *Crystals* 8:285
88. Matsuda Y, Shimahara H. 2007. *J. Phys. Soc. Jpn.* 76:051005
89. Kenzelmann M. 2017. *Rep. Prog. Phys.* 80:034501
90. Bergk B, Demuer A, Sheikin I, Wang Y, Wosnitza J, et al. 2011. *Phys. Rev. B* 83:064506
91. Tsuchiya S, Yamada JI, Sugii K, Graf D, Brooks J, et al. 2015. *J. Phys. Soc. Jpn.* 84:034703
92. Lortz R, Wang Y, Demuer A, Bottger PHM, Bergk B, et al. 2007. *Phys. Rev. Lett.* 99:187002
93. Agosta C, Fortune N, Hannahs S, Gu S, Liang L, et al. 2017. *Phys. Rev. Lett.* 118:267001
94. Wright JA, Green E, Kuhns P, Reyes A, Brooks J, et al. 2011. *Phys. Rev. Lett.* 107:087002
95. Mayaffre H, Kramer S, Horvatic M, Berthier C, Miyagawa K, et al. 2014. *Nat. Phys.* 10:928–32
96. Agosta C, Jin J, Coniglio WA, Smith BE, Cho K, et al. 2012. *Phys. Rev. B* 85:214514
97. Tanatar M, Ishiguro T, Tanaka H, Kobayashi H. 2002. *Phys. Rev. B* 66:134503
98. Coniglio W, Winter L, Cho K, Agosta C, Fravel B, Montgomery LK. 2011. *Phys. Rev. B* 83:224507
99. Koutroulakis G, Kuhne H, Schlueter J, Wosnitza J, Brown S. 2016. *Phys. Rev. Lett.* 116:067003
100. Cho K, Smith BE, Coniglio WA, Winter LE, Agosta CC, Schlueter JA. 2009. *Phys. Rev. B* 79:220507(R)
101. Yonezawa S, Kusaba S, Maeno Y, Auban-Senzier P, Pasquier C, Jrome D. 2008. *Phys. Rev. Lett.* 100:117002
102. Gurevich A. 2010. *Phys. Rev. B* 82:184504
103. Cho CW, Yang J, Yuan N, Shen J, Wolf T, Lortz R. 2017. *Phys. Rev. Lett.* 119:217002
104. Gloos K, Modler R, Schimanski H, Bredl CD, Geibel C, et al. 1993. *Phys. Rev. Lett.* 70:501–4
105. Modler R, Gegenwart P, Lang M, Deppe M, Weiden M, et al. 1996. *Phys. Rev. Lett.* 76:1292–95
106. Yamashita A, Ishii K, Yokoo T, Akimitsu J, Hedo M, et al. 1997. *Phys. Rev. Lett.* 79:3771–74
107. Radovan HA, Fortune NA, Murphy TP, Hannahs ST, Palm EC, et al. 2003. *Nature* 425:51–55
108. Bianchi A, Movshovich R, Capan C, Pagliuso PG, Sarrao JL. 2003. *Phys. Rev. Lett.* 91:187004
109. Kenzelmann M, Strassle T, Niedermayer C, Sigrist M, Padmanabhan B, et al. 2008. *Science* 321:1652–54
110. Bloch I, Dalibard J, Zwerger W. 2008. *Rev. Mod. Phys.* 80:885–964
111. Ketterle W, Zwierlein M. 2008. *Riv. Nuovo Cimento* 164:247–422
112. Gurarie V, Radzihovsky L. 2007. *Ann. Phys.* 322:2–119
113. Giorgini S, Pitaevskii LP, Stringari S. 2008. *Rev. Mod. Phys.* 80:1215–74
114. Radzihovsky L, Sheehy D. 2010. *Rep. Prog. Phys.* 73:076501
115. Regal CA, Greiner M, Jin DS. 2004. *Phys. Rev. Lett.* 92:040403
116. Zwierlein MW, Stan CA, Schunck CH, Raupach SMF, Kerman AJ, Ketterle W. 2004. *Phys. Rev. Lett.* 92:120403
117. Kinast J, Hemmer SL, Gehm ME, Turlapov A, Thomas JE. 2004. *Phys. Rev. Lett.* 92:150402
118. Eagles DM. 1969. *Phys. Rev.* 186:456–63
119. Leggett A. 1980. In *Modern Trends in the Theory of Condensed Matter*, ed. A Pękalski, J Przystawa, Vol. 115, *Lect. Notes Phys.*, *Proceedings of the 16th Karpacz Winter School of Theoretical Physics*, *Karpacz*, *Poland*, *Feb. 19–Mar. 3*, *1979*, pp. 13–27. Berlin, Heidelberg: Springer
120. Nozieres P, Schmitt-Rink S. 1985. *J. Low Temp. Phys.* 59:195–211
121. Zwierlein MW, Schirotzek A, Schunck CH, Ketterle W. 2006. *Science* 311:492–96
122. Partridge GB, Li W, Kamar RI, Liao Ya, Hulet RG. 2006. *Science* 314:54
123. Shin Y, Zwierlein MW, Schunck CH, Schirotzek A, Ketterle W. 2006. *Phys. Rev. Lett.* 97:030401
124. Nascimbène S, Navon N, Chevy F, Salomon C. 2010. *New J. Phys.* 12:103026
125. Combescot R. 2001. *Europhys. Lett.* 55:150–56
126. Liu WV, Wilczek F. 2003. *Phys. Rev. Lett.* 90:047002
127. Bedaque PF, Caldas H, Rupak G. 2003. *Phys. Rev. Lett.* 91:247002
128. Caldas H. 2004. *Phys. Rev. A* 69:063602
129. Castorina P, Grasso M, Oertel M, Urban M, Zappalà D. 2005. *Phys. Rev. A* 72:025601
130. Sedrakian A, Mur-Petit J, Polls A, Müther H. 2005. *Phys. Rev. A* 72:013613

131. Sheehy DE, Radzihovsky L. 2006. *Phys. Rev. Lett.* 96:060401
132. Pao CH, Wu ST, Yip SK. 2006. *Phys. Rev. B* 73:132506
133. Son DT, Stephanov MA. 2006. *Phys. Rev. A* 74:013614
134. Bulgac A, Forbes MM, Schwenk A. 2006. *Phys. Rev. Lett.* 97:020402
135. Sheehy DE, Radzihovsky L. 2007. *Ann. Phys.* 322:1790–924
136. Parish MM, Marchetti FM, Lamacraft A, Simons BD. 2007. *Nat. Phys.* 3:124–28
137. Radzihovsky L, Vishwanath A. 2009. *Phys. Rev. Lett.* 103:010404
138. Radzihovsky L. 2011. *Phys. Rev. A* 84:023611
139. Liao Ya, Rittner ASC, Paprotta T, Li W, Partridge GB, et al. 2010. *Nature* 467:567
140. Revelle MC, Fry JA, Olsen BA, Hulet RG. 2016. *Phys. Rev. Lett.* 117:235301
141. Parish MM, Baur SK, Mueller EJ, Huse DA. 2007. *Phys. Rev. Lett.* 99:250403
142. Zhang SC. 1998. *J. Phys. Chem. Solids* 59:1774–79
143. Raczkowski M, Capello M, Poilblanc D, Frésard R, Oleś AM. 2007. *Phys. Rev. B* 76:140505
144. Capello M, Raczkowski M, Poilblanc D. 2008. *Phys. Rev. B* 77:224502
145. Loder F, Kampf AP, Kopp T. 2010. *Phys. Rev. B* 81:020511
146. Wårdh J, Granath M. 2017. *Phys. Rev. B* 96:224503
147. Wårdh J, Andersen BM, Granath M. 2018. *Phys. Rev. B* 98:224501
148. Lee SS, Lee PA, Senthil T. 2007. *Phys. Rev. Lett.* 98:067006
149. Soto-Garrido R, Fradkin E. 2014. *Phys. Rev. B* 89:165126
150. Wu C, Sun K, Fradkin E, Zhang SC. 2007. *Phys. Rev. B* 75:115103
151. Soto-Garrido R, Cho GY, Fradkin E. 2015. *Phys. Rev. B* 91:195102
152. Granath M, Oganesyan V, Kivelson SA, Fradkin E, Emery VJ. 2001. *Phys. Rev. Lett.* 87:167011
153. Sikkema AE, Affleck I, White SR. 1997. *Phys. Rev. Lett.* 79:929–32
154. Zachar O, Tsvelik AM. 2001. *Phys. Rev. B* 64:033103
155. Zachar O. 2001. *Phys. Rev. B* 63:205104
156. Berg E, Fradkin E, Kivelson SA. 2010. *Phys. Rev. Lett.* 105:146403
157. Cho GY, Soto-Garrido R, Fradkin E. 2014. *Phys. Rev. Lett.* 113:256405
158. Jaefari A, Fradkin E. 2012. *Phys. Rev. B* 85:035104
159. Huang EW, Mendl CB, Jiang HC, Moritz B, Devereaux TP. 2018. *NPJ Quantum Mater.* 3:22
160. Verstraete F, Murg V, Cirac J. 2008. *Adv. Phys.* 57:143–224
161. Corboz P, White SR, Vidal G, Troyer M. 2011. *Phys. Rev. B* 84:041108
162. Corboz P, Rice TM, Troyer M. 2014. *Phys. Rev. Lett.* 113:046402
163. Dodaro JF, Jiang HC, Kivelson SA. 2017. *Phys. Rev. B* 95:155116
164. Jiang HC, Weng ZY, Kivelson SA. 2018. *Phys. Rev. B* 98:140505
165. Jiang HC, Devereaux T. 2018. Superconductivity in the Hubbard model and its interplay with charge stripes and next-nearest hopping t'. arXiv:1806.01465
166. Xu XY, Law KT, Lee PA. 2019. *Phys. Rev. Lett.* 122:167001
167. Hartnoll SA, Lucas A, Sachdev S. 2019. *Holographic Quantum Matter*. Cambridge, MA: MIT Press
168. Flauger R, Pajer E, Papanikolaou S. 2011. *Phys. Rev. D* 83:064009
169. Cremonini S, Li L, Ren J. 2017. *J. High Energy Phys.* 2017:81
170. Cremonini S, Li L, Ren J. 2017. *Phys. Rev. D* 95:041901
171. Cai RG, Li L, Wang YQ, Zaanen J. 2017. *Phys. Rev. Lett.* 119:181601
172. Chandrasekhar BS. 1962. *Appl. Phys. Lett.* 1:7
173. Clogston AM. 1962. *Phys. Rev. Lett.* 9:266–67
174. Sarma G. 2002. *J. Phys. Chem. Solids* 24:1029–32
175. Carlson J, Reddy S. 2005. *Phys. Rev. Lett.* 95:060401
176. Regal CA, Jin DS. 2003. *Phys. Rev. Lett.* 90:230404
177. Nikolić P, Sachdev S. 2007. *Phys. Rev. A* 75:033608
178. Veillette MY, Sheehy DE, Radzihovsky L. 2007. *Phys. Rev. A* 75:043614
179. Nishida Y, Son DT. 2006. *Phys. Rev. Lett.* 97:050403
180. Alford M, Bowers JA, Rajagopal K. 2001. *Phys. Rev. D* 63:074016
181. Bowers JA, Rajagopal K. 2002. *Phys. Rev. D* 66:065002

182. Machida K, Nakanishi H. 1984. *Phys. Rev. B* 30:122–33
183. Burkhardt H, Rainer D. 1994. *Ann. Phys.* 506:181–94
184. Matsuo S, Higashitani S, Nagato Y, Nagai K. 1998. *J. Phys. Soc. Jpn.* 67:280–89
185. Yoshida N, Yip SK. 2007. *Phys. Rev. A* 75:063601
186. Mora C, Combescot R. 2005. *Phys. Rev. B* 71:214504
187. Sheehy DE, Radzihovsky L. 2007. *Phys. Rev. B* 75:136501
188. Su WP, Schrieffer JR, Heeger AJ. 1979. *Phys. Rev. Lett.* 42:1698–701
189. Orso G. 2007. *Phys. Rev. Lett.* 98:070402
190. Hu H, Liu XJ, Drummond PD. 2007. *Phys. Rev. Lett.* 98:070403
191. Yang K. 2001. *Phys. Rev. B* 63:140511
192. Zhao E, Liu WV. 2008. *Phys. Rev. A* 78:063605
193. Radzihovsky L. 2012. *Phys. C: Supercond.* 481:189–206
194. Shimahara H. 1998. *J. Phys. Soc. Jpn.* 67:1872–75
195. de Gennes PG, Prost J. 1993. *The Physics of Liquid Crystals*. Oxford, UK: Oxford Univ. Press. 2nd ed.
196. Chaikin PM, Lubensky TC. 1995. *Principles of Condensed Matter Physics*. Cambridge, UK: Cambridge Univ. Press
197. Grinstein G, Pelcovits RA. 1981. *Phys. Rev. Lett.* 47:856–59
198. Samokhin K. 2010. *Phys. Rev. B* 81:224507
199. Samokhin K. 2011. *Phys. Rev. B* 83:094514
200. Agterberg DF, Kaur RP. 2007. *Phys. Rev. B* 75:064511
201. Dimitrova O, Feigel'man MV. 2007. *Phys. Rev. B* 76:014522
202. Gor'kov LP, Rashba EI. 2001. *Phys. Rev. Lett.* 87:037004
203. Frigeri PA, Agterberg DF, Koga A, Sigrist M. 2004. *Phys. Rev. Lett.* 92:097001
204. Cho GY, Bardarson JH, Lu YM, Moore JE. 2012. *Phys. Rev. B* 86:214514
205. Barzykin V, Gor'kov LP. 2002. *Phys. Rev. Lett.* 89:227002
206. Mineev V, Samokhin K. 1994. *Zh. Eksp. Teor. Fiz.* 105:747–63
207. Agterberg D. 2002. *Physica C* 387:13–16
208. Mineev V, Samokhin K. 2008. *Phys. Rev. B* 78:144503
209. Smidman M, Salamon M, Yuan H, Agterberg D. 2017. *Rep. Prog. Phys.* 80:036501
210. Hart S, Ren H, Kosowsky M, Ben-Shach G, Leubner P, et al. 2016. *Nat. Phys.* 13:87
211. Michaeli K, Potter AC, Lee PA. 2012. *Phys. Rev. Lett.* 108:117003
212. Fu L, Kane CL. 2008. *Phys. Rev. Lett.* 100:096407
213. Santos L, Neupert T, Chamon C, Mudry C. 2010. *Phys. Rev. B* 81:184502
214. Chen AQ, Park MJ, Gill ST, Xiao Y, Reig-i-Plessis D, et al. 2018. *Nat. Commun.* 9:3478
215. Bednik G, Zyuzin AA, Burkov AA. 2015. *Phys. Rev. B* 92:035153
216. Li Y, Haldane FDM. 2018. *Phys. Rev. Lett.* 120:067003
217. Wang Y, Ye P. 2016. *Phys. Rev. B* 94:075115
218. He RH, Tanaka K, Mo SK, Sasagawa T, Fujita M, et al. 2008. *Nat. Phys.* 5:119–23
219. Vishik IM, Lee WS, He RH, Hashimoto M, Hussain Z, et al. 2010. *New J. Phys.* 12:105008
220. Lee WS, Vishik IM, Tanaka K, Lu DH, Sasagawa T, et al. 2007. *Nature* 450:81–84
221. Renner C, Revaz B, Genoud JY, Kadowaki K, Fischer Ø. 1998. *Phys. Rev. Lett.* 80:149–52
222. Berg E, Altman E. 2007. *Phys. Rev. Lett.* 99:247001
223. Parham S, Li H, Nummy TJ, Waugh JA, Zhou XQ, et al. 2017. *Phys. Rev. X* 7:041013
224. Hashimoto M, Nowadnick EA, He RH, Vishik IM, Moritz B, et al. 2014. *Nat. Mater.* 14:37–42
225. Dai Z, Lee PA. 2017. *Phys. Rev. B* 95:014506
226. Kapitulnik A, Kivelson SA, Spivak B. 2019. *Rev. Mod. Phys.* 91:011002
227. Zelli M, Kallin C, Berlinsky AJ. 2012. *Phys. Rev. B* 86:104507
228. Wang L, Vafek O. 2013. *Phys. Rev. B* 88:024506
229. Norman MR, Davis JCS. 2018. *PNAS* 115:5389–91
230. Kacmarcik J, Vinograd I, Michon B, Rydh A, Demuer A, et al. 2018. *Phys. Rev. Lett.* 121:167002
231. Li L, Wang Y, Komiya S, Ono S, Ando Y, et al. 2010. *Phys. Rev. B* 81:054510
232. Yu F, Hirschberger M, Loew G, Lawson B, Asaba T, et al. 2016. *PNAS* 113:12667–72

233. Lee PA. 2019. *Phys. Rev. B* 99:035132
234. Blackburn E. 2013. Presented at the 2019 Gordon Res. Conf., Les Diablerets, Switzerland
235. Peng YY, Salluzzo M, Sun X, Ponti A, Betto D, et al. 2016. *Phys. Rev. B* 94:184511
236. Chaix L, Ghiringhelli G, Peng YY, Hashimoto M, Moritz B, et al. 2017. *Nat. Phys.* 13:952–56
237. Stengen Z, Han SJ, Wu J, Pramanik AK, Hücker M, et al. 2013. *Phys. Rev. B* 87:064509

Annual Review of Condensed Matter Physics

Volume 11, 2020

Contents